PRESIDENCY UNIVERSITY

DEPARTMENT OF LIFE SCIENCES

Ph.D. Thesis Synopsis

Characterizing the antibacterial and anti-inflammatory properties of silver nanoparticle synthesized using *Syzygium aromaticum* against *Staphylococcus aureus*

Name of Candidate: Sima Sikdar

Registration Number with date: R-18RS18220179, 11th February, 2020

Name of Supervisor: Mausumi Sikdar (née Bhakta)

Name: Sima Sikdar

Supervisor: Dr. Mausumi Sikdar (née Bhakta)

Title of Thesis: Characterizing the antibacterial and anti-inflammatory properties of silver nanoparticle synthesized using *Syzygium aromaticum* against *Staphylococcus aureus*

PhD registration Number with date: R-18RS18220179, 11th February, 2020

Enrolment Number with date: PU/PHD/DLS/2018/097, 31.10.2018

Place of work: Presidency University, Kolkata

Residential Address: Vill+ P.O: Pakuahat, Dist: Malda, P.S.: Bamangola, Pin: 732138

Corresponding Address: Presidency University, Department of Life Sciences, Kolkata- 700073

Email: simasikdar29@gmail.com

Phone Number: 9064347188

Sima Sikdar 19.03.24

Signature of Research Scholar

Msikda 19/3/2024

Signature of Supervisor

Contents

1. Abstract 6
2. Introduction 6
3. Objectives of the work plan 7
4. Methodology 7
4.1. Preparation of clove extract 7
4.2. Optimization of green synthesis of silver nanoparticles 8
4.3. Characterization of the properties of silver nanoparticles 8
4.4. Collection of bacterial strains 8
4.5. Identification of bacterial strains by biochemical methods and genetic method 8
4.6. Identification of bacterial genes 9
4.7. Antibiotic susceptibility test 9
4.8. Evaluation of the antibacterial activity of the green synthesized AgNPs against *S. aureus* 10
4.9. Effect of AgNPs on growth curve 10
4.10. Evaluation of bacterial cell membrane integrity 10
4.11. Evaluation of the morphological structure of *S. aureus* 10
4.12. Fluorescence microscopy (Observation of live and dead bacterial cells) 10
4.13. Quantification of bacterial dead-live cells using fluorescence-activated cell sorting (FACS) 10
4.14. Single-cell gel electrophoresis (Comet assay) 11
4.15. Photocatalytic activity of silver nanoparticle 11
4.16. Animal experimental design 11
4.17. Body weight, Organ collection, Blood Collection, Hematology and Biochemical Assay 12
4.18. Statistical analysis 12
4.19. Histopathological analysis 12
5. Results 12
5.1. Optimization of AgNPs synthesis by UV-visible spectroscopy 12
5.2. XRD analysis 14
5.3. TEM analysis 16
5.4. AFM images of AgNPs 17
5.5. FTIR analysis 17
5.6. Hydrodynamic size analysis 19

5.7. Zeta potential analysis 19
5.8. Bacterial strains collection and identification 20
5.8.1. Biochemical test results 20
5.8.2. Genetic identification of bacterial strains 21
5.9. Phylogenetic analysis 22
5.10. Identification of bacterial genes 22
5.11. Antibiotic susceptibility test 23
5.12. Antimicrobial activity of AgNPs by agar well diffusion method 24
5.13. Results of quantitative study 26
5.14. Effect of AgNPs on growth curve 27
5.15. Bacterial cell membrane damage 27
5.16. Bacterial surface morphology study using AFM 29
5.17. Fluorescence microscopy (demonstration of live and dead bacterial cells) 30
5.18. Single-cell gel electrophoresis (comet assay) 32
5.19. Quantification of bacterial death using FACS 33
5.20. Photocatalytic degradation 35
5.21. Bacterial load in animal model 36
5.22. Animal weight 37
5.23. Organ index 37
5.24. Knee joint diameter 37
5.25. Morphological analysis of knee joint 38
5.26. Blood parameters 38
5.27. Biochemical findings 39
5.28. Effect on inflammatory marker 40
5.29. Histological analysis 41
5.29.1. Knee joint 41
5.29.2. Liver 42
5.28.3. Kidney 43
5.28.4. Spleen 45
5.30. Microscopic grading and scoring 46
6. Conclusion/Discussion 47
7. Significance of this study 51
8. Future directions 52

9. References.....52

11. Plagiarism Certificate form Turnitin

12. Additional Documents:

Certificate of conferences attended

First page of published manuscript

Certificates of ethical clearances

Characterizing the antibacterial and anti-inflammatory properties of silver nanoparticle synthesized using *Syzygium aromaticum* against *Staphylococcus aureus*

1. Abstract

This study utilized *Syzygium aromaticum* for the environmentally friendly production of silver nanoparticles (AgNPs), aiming to optimize conditions for efficient synthesis and investigate their antibacterial and photocatalytic properties. The antibacterial effects against *Staphylococcus aureus* were demonstrated and AgNPs' role in damaging bacterial membranes was confirmed through various microscopy techniques. Characterization of AgNPs involved UV–visible spectrophotometry, X-ray diffraction (XRD), transmission electron microscopy (TEM), atomic force microscopy (AFM), dynamic light scattering (DLS), zeta potential analysis and Fourier transform infrared spectroscopy (FTIR). AgNPs exhibited significant malachite green (MG) degradation (97.21%) at a rate of 0.034±0.005 min^{-1}, highlighting their versatility in wastewater treatment. The investigation further explored the therapeutic efficacy of green-synthesized AgNPs against *Staphylococcus aureus*-induced septic arthritis in adult male Wistar rats. Over 14 days, rats were divided into six groups and the impact of AgNPs, vancomycin and their combination were monitored. The arthritis control group exhibited elevated serum enzymes, markers, inflammation and histological injury. Conversely, treated groups showed reduced inflammation and histological improvements. The combination of vancomycin and AgNPs not only restored enzyme and marker levels but also mitigated cell damage by effectively reducing the bacterial septic arthritis. This study highlights the potential therapeutic effectiveness of vancomycin and AgNPs in alleviating the effects of *Staphylococcus aureus*-induced septic arthritis.

2. Introduction

In recent years, nanoparticles (NPs) have gained immense significance across diverse fields due to their unique properties [1] [2]. Silver nanoparticles (AgNPs) are particularly noteworthy for their potent antimicrobial effects [3] [4]. Traditional NP synthesis methods often involve toxic components, leading to the emergence of greener synthesis methods using microorganisms and plant extracts [5] [6]. This study focuses on the green synthesis of AgNPs using *Syzygium aromaticum*, known for its phytochemical content, enhancing safety and efficacy [7]. The antibacterial mechanism of AgNPs involves various interactions, including silver ions, DNA replication disruption, thiol group inactivation and reactive oxygen species production [6].

Septic arthritis, which is mainly caused by *Staphylococcus aureus,* is the most serious condition in the differential diagnosis of an inflamed, swollen joint [8]. The moment *S. aureus* enters the joint cavity, an immediate immune reaction is set out. Even after receiving prompt therapy, the patients frequently experience lifelong joint dysfunction because the damage to their joints is generally irreversible [9]. So, this study poses a significant health challenge, prompting the exploration of AgNPs in combination with vancomycin for septic arthritis treatment. Additionally, the study addresses water pollution, particularly from dyeing industries, by investigating the photocatalytic degradation facilitated by green-synthesized NPs. This approach offers a promising solution without the use of hazardous chemicals associated with conventional wastewater treatment methods.

Overall, this research focuses on the green synthesis of AgNPs using clove extract, optimizing the synthesis process, characterizing the NPs and assessing their antibacterial and photocatalytic activities. The findings hold promise for environmentally friendly wastewater treatment and innovative medical applications in combating bacterial infections and inflammatory conditions.

3. Objectives of the work plan

1. Green synthesis and characterization of green synthesized AgNPs using clove (*Syzygium aromaticum*).
2. Study of the effect of green synthesized AgNPs on *Staphylococcus aureus in vitro.*
3. Evaluation of the anti-inflammatory effect of green synthesized AgNPs on septic arthritis in rat model.

4. Methodology

4.1. Preparation of clove extract

Clove flower buds sourced from a Kolkata market in India, authenticated by the Botanical Survey of India (Reference: CNH/Tech.II/2023/, 28th February 2023), underwent preparation by the following method [10][11]. 5 g of clove powder was boiled with 100 mL of autoclaved distilled water and at 80˚C for 20 minutes [10]. The resulting extract was then centrifuged at 7000 rpm and stored at 4°C for future use.

4.2. Optimization of green synthesis of silver nanoparticles

AgNPs were produced by altering $AgNO_3$ salt concentration (0.50 mM, 0.75 mM, 1 mM and 1.50 mM), temperature (25, 40, 60 and 80 °C), *S. aromaticum* extract volume (4, 6, 8 and 10 mL), pH (7, 8, 9 and 10) and reaction times (10, 15, 20 and 25 min) to identify optimal synthesis conditions. The SPR peak nature was examined via UV-visible spectroscopy and Origin 8.5 software was used to plot the resulting data.

4.3. Characterization of the properties of silver nanoparticles

The formation of AgNPs was confirmed by the UV–visible spectrophotometer (Shimadzu UV 2450–PC). It gives a qualitative idea about the size and shape of the NPs by the position, width and shape of the SPR band [12][13]. XRD (PXRD Bruker D8 Advance) was done (2θ range of 30°–80°) to study the crystalline nature of the AgNPs. The size of the synthesized NPs was determined by TEM (high-resolution transmission electron microscope JEM2100, JEOL). The atomic force microscopy (AFM- Pico5500) was done to analyse the surface of AgNPs. The hydrodynamic size and zeta potential value of the AgNPs were determined by DLS (Malvern). The functional groups responsible for the green synthesis were determined by FTIR (Perkin Elmer, Frontier, USA). The resulting data was analyzed by the Origin pro 8.5, Pico view 1.2 and imageJ software.

4.4. Collection of bacterial strains

Bacterial strains were collected from 32 nasal nares samples of Presidency University students (22-26 years old), excluding those with recent illness or antibiotic use. Samples were streaked on 5% nutrient agar sodium chloride (NA-NaCl) plates and incubated for 24 hours.

4.5. Identification of bacterial strains by biochemical methods and genetic method

Bacterial strains were identified through Gram staining to differentiate between Gram-positive and Gram-negative bacteria. The catalase test was employed to detect catalase enzymes, indicative of potential *S. aureus* strains. Haemolysis activity was studied using blood agar plates (BAP), while Mannitol salt agar (MSA) plates, a selective differential medium for *Staphylococcus* species, were utilized. Further identification involved genetic methods, including 16S rDNA sequencing. A phylogenetic analysis was performed using the Neighbor-Joining method and was executed using MEGA 6 software. Additionally, a clinical *S. aureus* strain was obtained from the Calcutta School of Tropical Medicine in Kolkata, India.

4.6. Identification of bacterial genes

Specific genes related to *S. aureus* was isolated using the Thermofisher DNA isolation kit (**Table 1**). PCR reactions (Veriti Thermal Cycler, Applied Biosystems, CA, USA) were conducted in 50 µL volumes with specific components, including reaction buffer, dNTP mix, forward and reverse primers, template, Taq polymerase and milli-Q water.

Table 1: Specific genes in *S. aureus*

Genes	Reference numbers (Sigma Aldrich)	Expected size of DNA fragments
mecA	BA01358538	147 bp
nuc	BA01358536	270 bp
pvl	BA01358541	433 bp
SCCmec I	BA01358534	613 bp
tsst-1	BA01366325	326 bp

4.7. Antibiotic susceptibility test

Antibiotic susceptibility test was done by Kirby-Bauer method using the following antibiotics (**Table 2**).

Table 2: Different antibiotics and their dose

Antibiotics (Himedia)	Dose (mcg/disc)
Methicillin (MET)	5
Vancomycin (VAN)	30
Kanamycin (K)	30
Gentamicin (GEN)	10
Tetracycline (TET)	30
Ampicillin (AMP)	10
Chloramphenicol (C)	30
Amoxicillin (AT)	10
Rifamycin ®	15
Amikacin (AK)	30
Cefixime (CFM)	5
Norfloxacin (NX)	10

4.8. Evaluation of the antibacterial activity of the green synthesized AgNPs against *S. aureus*

Agar well diffusion assay, a quantitative study, was employed to assess the antibacterial activity of the synthesized AgNPs. This served as an initial screening, prompting further evaluation of antibacterial efficacy using the Minimum Inhibitory Concentration (MIC) value, denoting the lowest agent concentration inhibiting bacterial growth through serial dilution [14].

4.9. Effect of AgNPs on growth curve

S. aureus was cultured in 100 ml of LB medium to achieve an OD600 nm of 0.1. The culture was exposed to both MIC and sub-MIC concentrations of AgNPs at 37°C. The growth of *S. aureus* was monitored by measuring OD at 600 nm using intervals 0 h, 1 h, 2 h, 3 h, 4 h, 5 h and 6 h [15]. The percentage of growth inhibition was calculated by the following formula, Growth inhibition percentage (%)= [1- (treated OD600 nm/ control OD600 nm)] ×100 [16].

4.10. Evaluation of bacterial cell membrane integrity

The assessment was conducted using scanning electron microscopy (SEM-Model EVO18 Special edition, Carl Zeiss) for membrane damage, with a concentration of 31.25 μg/mL AgNPs and varying exposure times (2, 4, and 6 hours) [17].

4.11. Evaluation of the morphological structure of *S. aureus*

Additionally, atomic force microscopy (AFM) was employed to study the morphological structure of *S. aureus* treated with 31.25 μg/mL AgNPs for 2 hours and examined using AFM (Pico5500) [18].

4.12. Fluorescence microscopy (Observation of live and dead bacterial cells)

Live and dead bacterial cells were assessed using a double staining method with Acridine Orange (AO) and Ethidium Bromide (EB) and observed under a fluorescence microscope (Zeiss Axioscope A1, Thornwood, NY, USA). The fluorescent images were then analyzed using ImageJ software (ij153-win-java8) to measure fluorescent intensity.

4.13. Quantification of bacterial dead-live cells using fluorescence-activated cell sorting (FACS)

The quantification was done using PI staining which was used to distinguish dead cells and the viable cells. The experimental setup included five samples: a buffer-only sample, an unstained

sample, a control group stained with PI and two treated groups exposed to sub-MIC and MIC concentrations of AgNPs for 2h [19] [20].

4.14. Single-cell gel electrophoresis (Comet assay)

Bacterial cells were stained with PI after the treatment with Vancomycin (VCN), AgNPs (AgNPs), their combination (VNPs) and H_2O_2 for 2 hours. Cells were examined using a Zeiss Axioscope A1 fluorescence microscope. DNA breaks were quantified using Comet Assay Software Project (CASP).

4.15. Photocatalytic activity of silver nanoparticle

A concentration of 0.5 mg/mL of AgNPs was used for dye degradation at 0, 30, 60 and 90-minute intervals. UV-Visible spectroscopy (500-700 nm) monitored the reaction progress. The degradation efficiency was calculated using the formula: Degradation efficiency (%) = $(A_0 - A_t)/A_0 \times 100$, where A_0 is the initial absorbance and A_t is the absorbance at specific time intervals (30, 60 and 90 minutes) [21] [22] [23].

4.16. Animal experimental design

This study involved 48 male Wistar rats (150-200 gm) adhering to ethical guidelines set by the Institutional Animal Ethics Committee of Presidency University and the Committee for the Purpose of Control and Supervision of Experiments on Animals, Ministry of Environment, Forest and Climate Change, Government of India. The rats were randomly divided into six groups, each with eight animals (**Table 3**). After 24 hours of bacterial intraarticular injection, drugs were intraarticularly injected. Treatments, based on previous studies (**Table 3**), were administered for three doses on day 2, 6 and 10. After 14 days, animals were sacrificed and further experiment was done.

Table 3: Different groups of animals and their conditions

Groups	**Conditions**	**Intraarticular injection dose** (0.1 mL into the left stifle joint of rats)
Group I	Normal healthy control (NC)	Normal saline was injected
Group II	AgNPs injected without bacteria (NP)	0.3 mg/kg [24] [25]
Group III	*S. aureus* injected arthritis control (AC)	(1×10^3 CFU/knee) [26]

Group IV	Rats treated with AgNPs (TNPs)	0.3 mg/kg [24] [25]
Group V	Rats treated with Vancomycin (VCM)	13 mg/kg [26]
Group VI	Rats treated with VCM and AgNPs (VNP)	Treated with VNPs (Vancomycin 13 mg/kg + 0.3 mg/kg AgNPs) as the doses mentioned above where AgNPs were given after 2 h of antibiotic treatment [27]

4.17. Body weight, Organ collection, Blood Collection, Hematology and Biochemical Assay

The weight of the animals was recorded on days 0, 7 and 14. Following sacrifice, the organs were collected. The hematological parameters, including WBC, neutrophil, lymphocyte and RBC counts were analyzed using an automatic fully digital hematology analyzer. Biochemical assays for ALT, AST, creatinine, total protein, IL-6 and CRP concentrations were conducted in the plasma using commercial kits from ABclonal, India.

4.18. Statistical analysis

The data are presented as mean ± SE and analyzed using SPSS software. Statistical significance among groups was assessed by one-way ANOVA followed by Tukey's multiple comparison test. P values ≤ 0.05 were considered statistically significant.

4.19. Histopathological analysis

All 48 rats were sacrificed after ketamine hydrochloride (87 mg/kg) anesthesia. Liver, kidney, spleen and knee joint tissues were fixed, embedded and sectioned for histological examination [28]. A semi-quantitative grading system ranging from 0 (normal) to 4 (severe pathology) was employed, with grades indicating the extent of tissue damage on a five-point ordinal scale: (0) none, (1) mild< 25%, (2) moderate 25%-50%, (3) severe 50%-75% and (4) extensive severe>75% tissue damage [29][30].

5. Results

5.1. Optimization of AgNPs synthesis by UV-visible spectroscopy

The absorbance peak intensity varied with different salt concentration, temperature, extract volume, pH and reaction time (**Figure 1A-E**). The blue shift of the peak indicates the formation of smaller size NPs and the red shift indicates the formation of larger size NPs. Increased salt concentration (1 mM), a temperature of 40˚C, higher extract volume (10 mL), pH 10 and a reaction time of 25 minutes resulted in smaller-sized AgNPs as shown in **Figure 1A-E**. The optimum synthesis of AgNPs produced a brownish-yellow solution with a characteristic absorbance peak at approximately 406 nm, confirming their presence (**Figure 1F**) [31]**,** [32]. The findings from UV-visible spectroscopy were additionally validated and illustrated in **Figure 2**.

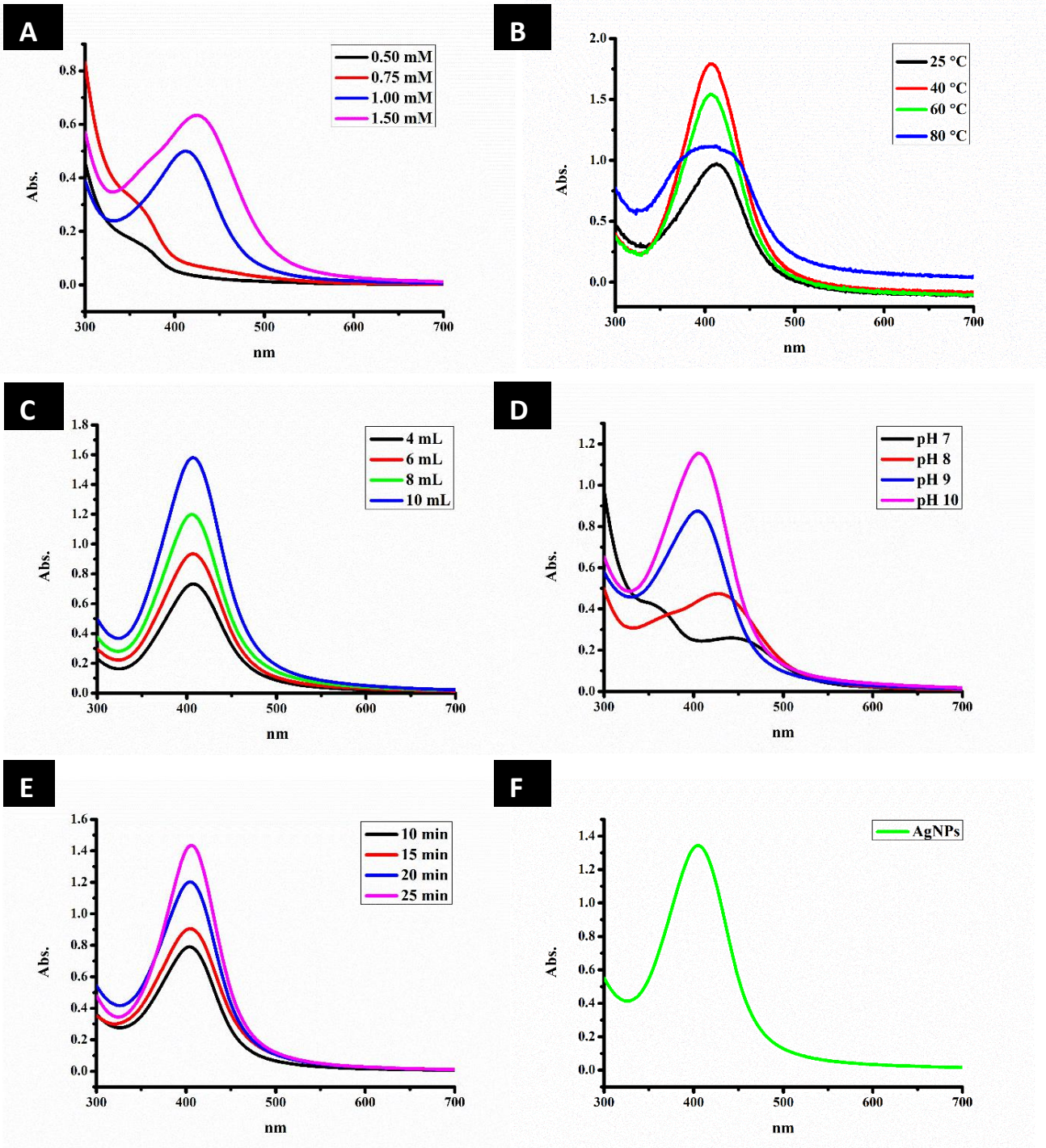

Figure 1 illustrates the enhancement of the eco-friendly production of AgNPs using UV-Visible spectroscopy. **A:** Examining the impact of salt concentration, **B:** Investigating the influence of temperature, **C:** Analyzing the effect of extract volume, **D:** Evaluating the impact of pH, **E:** Studying the influence of time, **F:** Describing the characterization of the produced AgNPs through UV-Visible spectroscopy under the optimal conditions identified in this research.

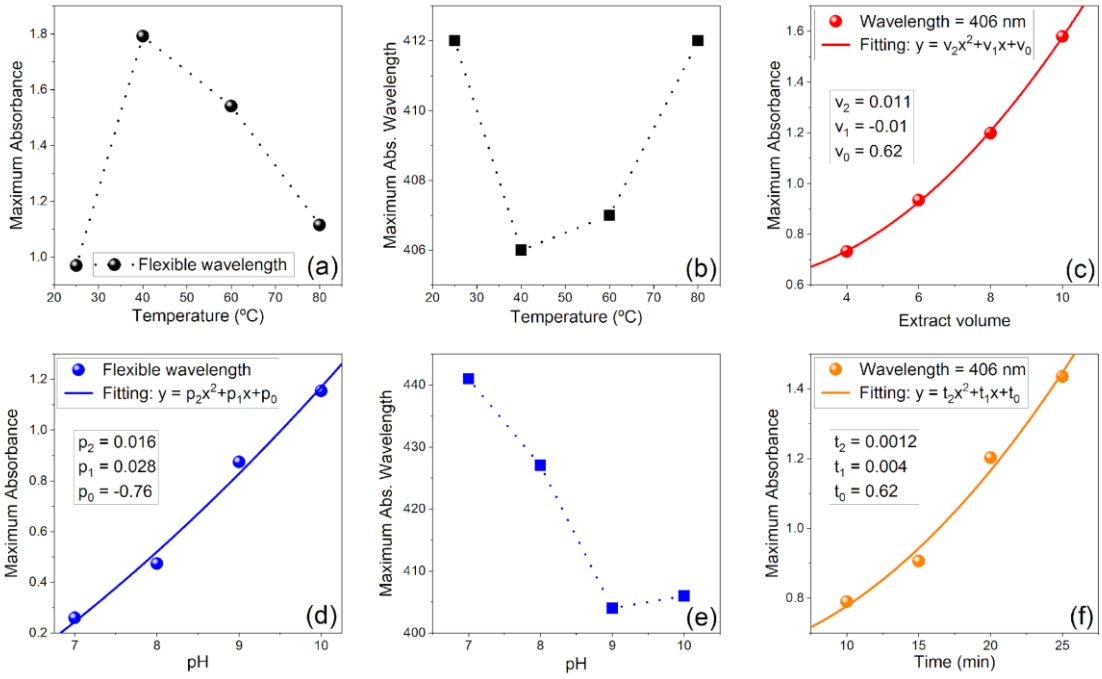

Figure 2 (a) the relationship between maximum absorbance and temperature, along with **(b)** the corresponding wavelengths. Additionally, **(c)** illustrates the variation in maximum absorbance concerning extract volume, while **(d)** showcases the correlation between maximum absorbance and pH of the reaction mixture, along with **(e)** the associated wavelengths. Lastly, **(f)** portrays the dependence of maximum absorbance on reaction time. The symbols in the figure represent experimental data points, with solid lines indicating second-degree polynomial fittings. Broken lines are included as linear guides for the data. Notably, the wavelength (~406 nm) linked to the peak absorption remains independent of changes in extract volume and reaction time.

5.2. XRD analysis

2θ values of 38.5198, 44.6471, 64.8378 and 77.7537 degrees (**Figure 3**), were identified in XRD indicating silver metal and corresponded to the crystallographic planes (111), (200), (220) and (311). The face-centered cubic (FCC) arrangement of NPs was confirmed through

XRD spectrum analysis using the Scherrer equation. The average particle size of the bio-inspired silver NPs was determined (**Table 4**) using the formula $D = K\lambda/\beta COS\theta$, where K is the shape constant, λ is the X-ray wavelength, β is the full-width half maximum and θ is the peak position [33].

Table 4: Average particle size of the green synthesized AgNPs was calculated using Scherrer's equation.

Peak number	**FWHM**	**2θ**	**θ**	**θ (radian)**	**FWHM (radian)**	**Cosθ**	**βCosθ**	**kλ**	**Size (nm)**
Peak 1	0.60664	38.50654	19.25327	0.335863	0.005859	0.944126	0.005532	0.138654	25.07
Peak 2	0.94254	44.63581	22.31791	0.389323	0.006792	0.925166	0.006283	0.138654	22.07
Peak 3	0.62076	64.84842	32.42421	0.565622	0.009867	0.844255	0.00833	0.138654	16.64
Peak 4	0.89169	77.77894	38.88947	0.678405	0.011834	0.778575	0.009214	0.138654	15.05
Average size									19.71

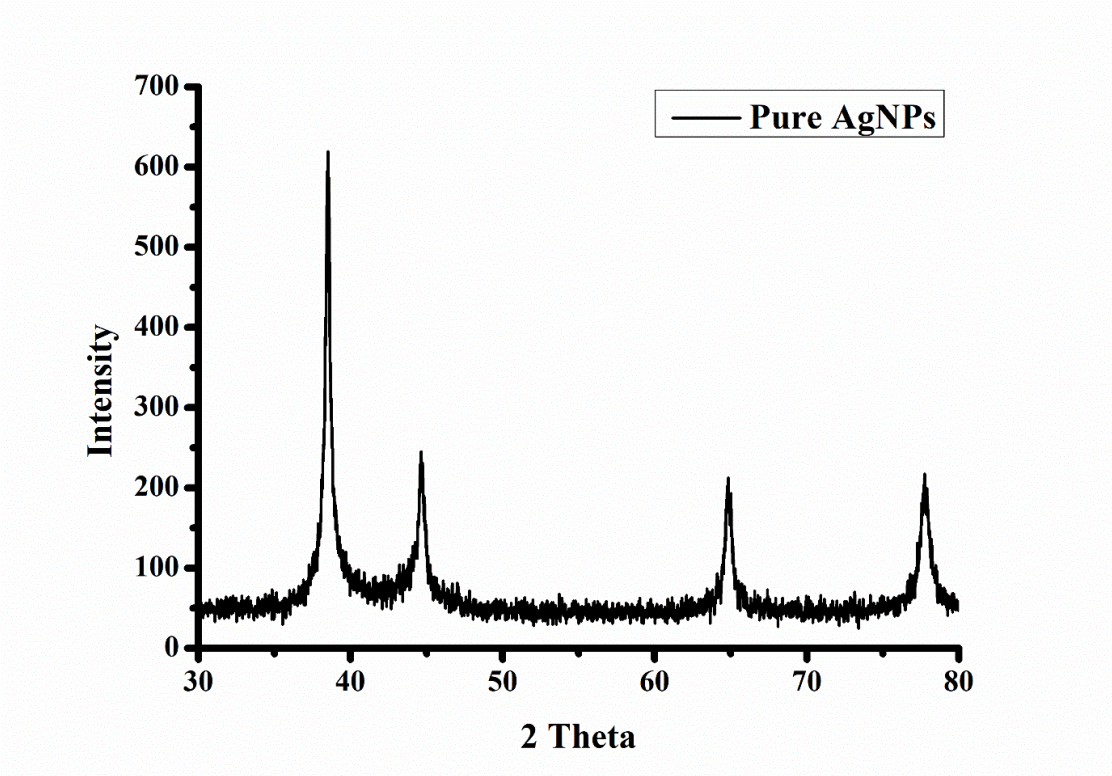

Figure 3 XRD examination of the green synthesized AgNPs

5.3. TEM analysis

The synthesized NPs were spherical with a size of 12.34 ± 1.90 nm (**Figure 4**), showing slight agglomeration. Selected Area Electron Diffraction (SAED) analysis verified the crystalline nature of the AgNPs, showing distinct crystal planes (111, 200, 220, and 311), characteristic of the face centred cubic (FCC) structure of elemental silver [34].

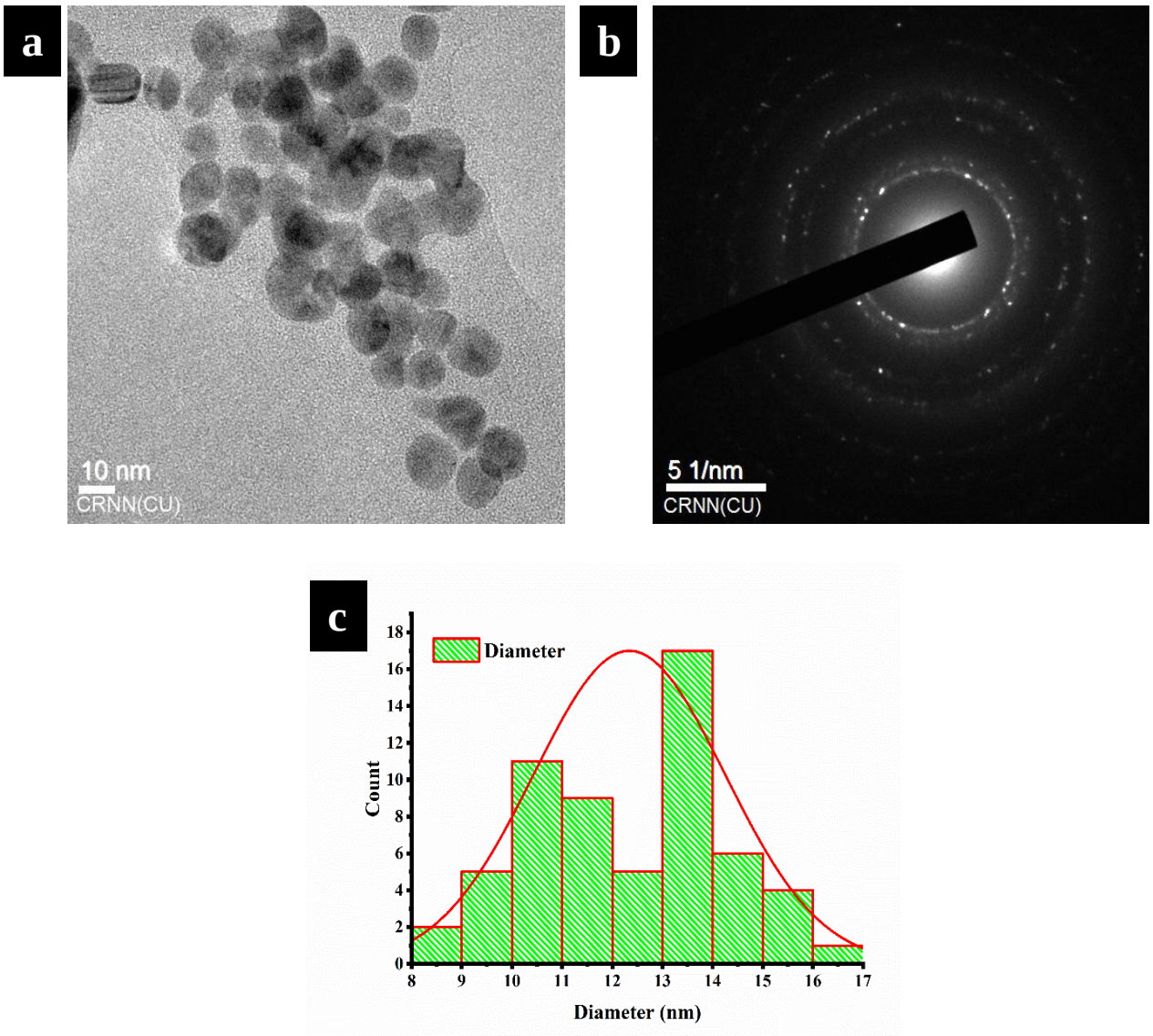

Figure 4 TEM analysis of the synthesized AgNPs. **(a)** Presents a TEM image of the AgNPs, **(b)** features Selected Area Electron Diffraction (SAED) patterns derived from the TEM image, validating the crystalline nature and exhibiting the (111), (200), (220) and (311) face-centered cubic (FCC) crystal planes of silver. **(c)** Displays a histogram outlining the size distribution of the AgNPs.

5.4. AFM images of AgNPs

AFM characterization stated about morphological structure of AgNPs in three dimensional forms. The 3D image shows that the particles are approximately spherical with aggregations (**Figure 5A**). Highly dispersed NPs have an average size range of 10–100 nm (**Figure 5C**). The average size was around 23.80 ± 9.55 (**Figure 5C**).

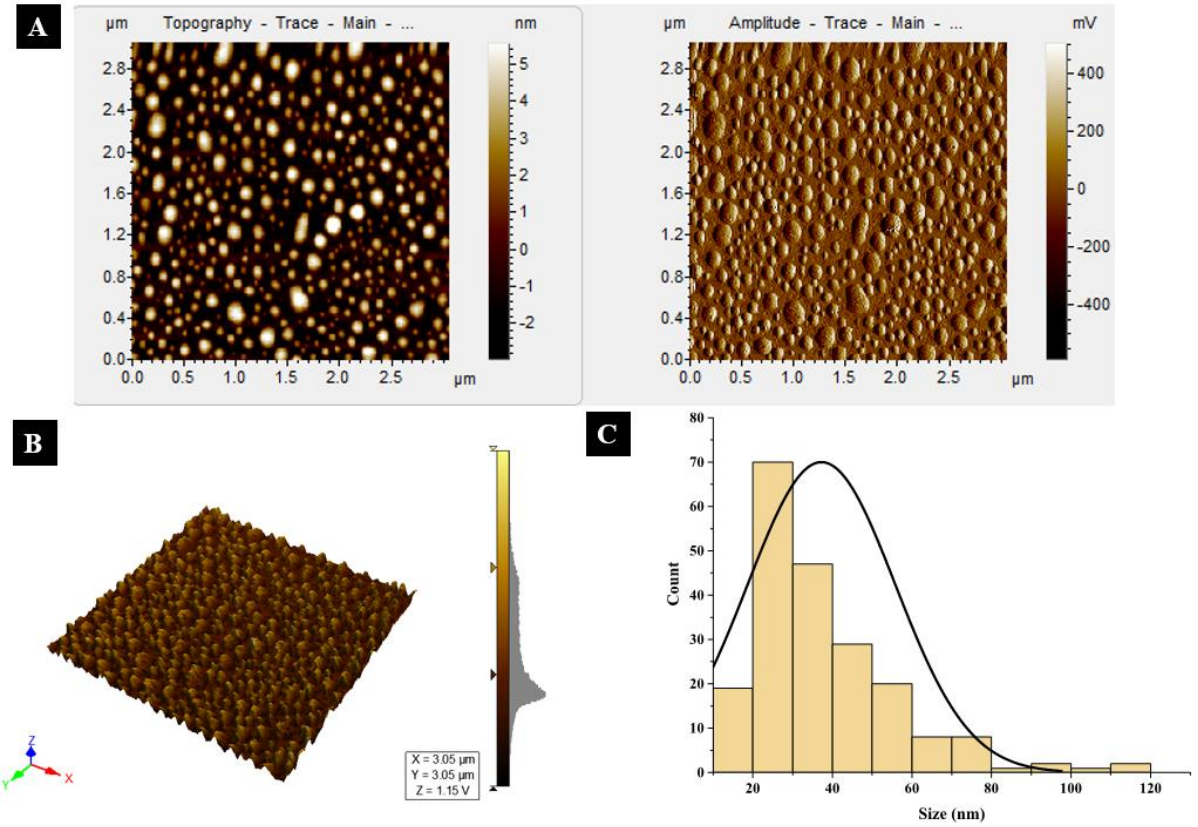

Figure 5 AFM images of AgNPs **A:** 2D topography and amplitude of AgNPs, **B:** The same topography in 3D. **C:** Histograms of the equivalent spherical particle diameter of the AgNPs.

5.5. FTIR analysis

The diverse phytochemical constituents present in the aqueous extract of clove helps in the reduction of $AgNO_3$ and capped the synthesized AgNPs as shown in **Figure 6**. The possible biomolecules are tabulated in **Table 5**.

Table 5: Results from FTIR analysis of both clove extract and the synthesized AgNPs

Wave number (cm^{-1})	Clove extract		Wave number (cm^{-1})	AgNPs	
	Bond/stretching	Functional group		Bond/stretching	Functional group

3402 cm^{-1}	O–H stretch and N–H stretch	phenols and amides [35], alcoholic group [36]	3438 cm^{-1}	O–H stretch and N–H stretch	phenols and amides [35], alcoholic group [36]
2096 cm^{-1}	-OH stretching and aliphatic -C-H stretching	aliphatic group [37]	2088 cm^{-1}	-OH stretching and aliphatic -C-H stretching	Aliphatic group [37]
1628 cm^{-1}	C=O stretching vibrations	amide groups, luteolin [35]	1627 cm^{-1}	C=O stretching vibrations	amide groups, luteolin [35]
1364	stretching deformation of (C-O) and phenolic (O–H) groups	phenols [38]	1342 cm^{-1}	C-H bending vibrations	phenols [38]
1039 cm^{-1}	C-N stretching vibration	aliphatic amines or alcohols, or phenols [39]	1032-1058 cm^{-1}	C-N stretching vibration	aliphatic amines or alcohols, or phenols [39]
721 cm^{-1}	N-H stretching	Primary/secondary amines [40]	714 cm^{-1}	N-H stretching	Primary/secondary amines [40]

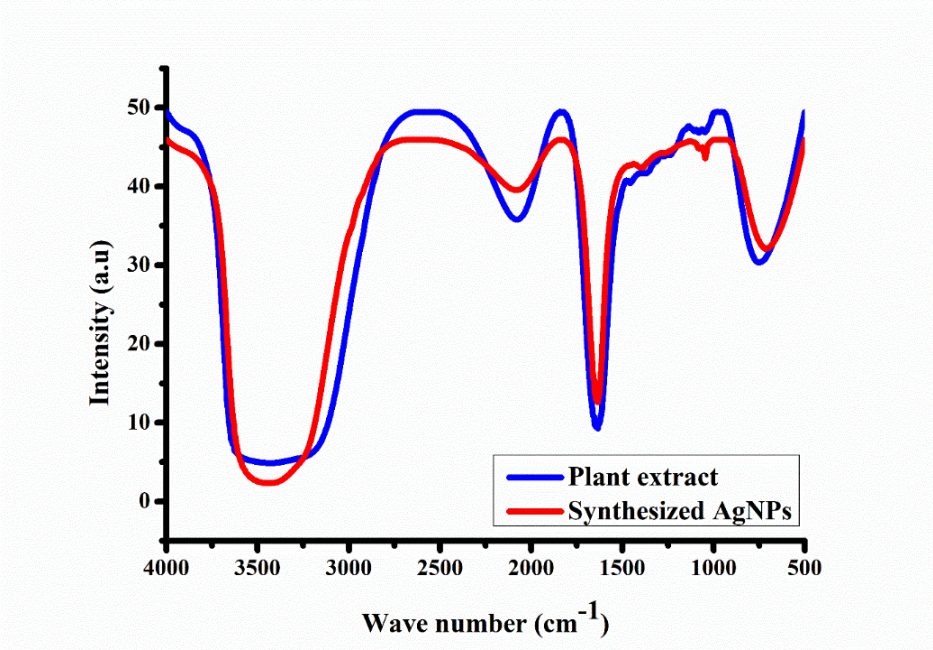

Figure 6 FTIR analysis of both clove extract and the synthesized AgNPs.

5.6. Hydrodynamic size analysis

DLS measurements revealed the hydrodynamic size of AgNPs and the average size of ~98% AgNPs was 52.05 ± 13.41 nm (**Figure 7**).

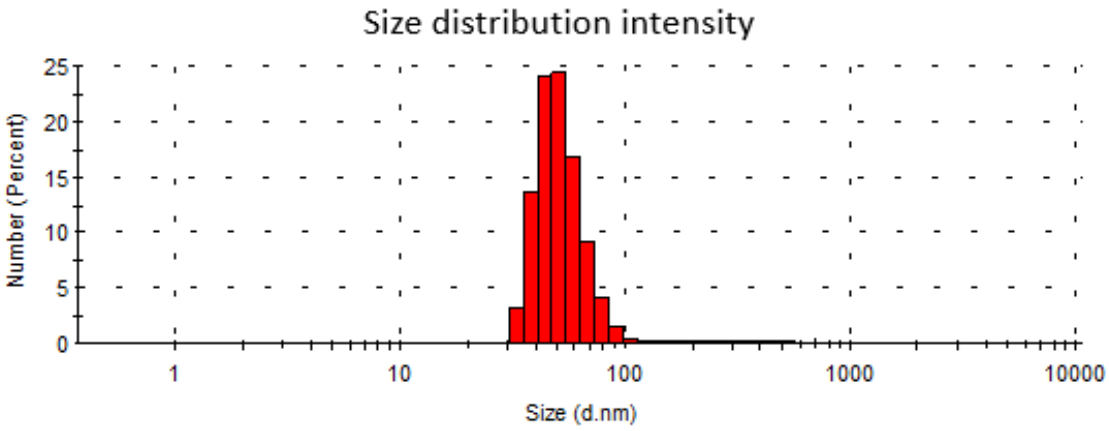

Figure 7 DLS size distribution of synthesized AgNPs

5.7. Zeta potential analysis

The synthesized AgNPs showed a zeta potential value of -18.6 mV (**Figure 8**). The negative zeta potential value of the synthesized AgNPs results in a robust repulsive force between particles, effectively preventing aggregation [41].

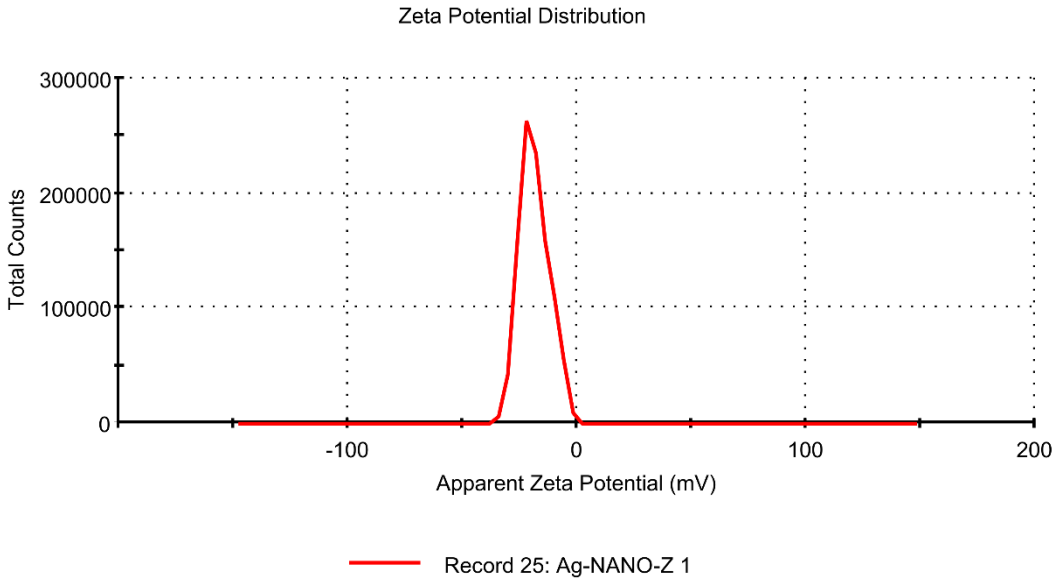

Figure 8 Zeta potential of synthesized AgNPs

5.8. Bacterial strains collection and identification

5.8.1. Biochemical test results

Out of the 32 strains collected, five bacterial strains (**Table 6**) were found to be Gram-positive cocci, arranged like a bunch of grapes, when observed under the microscope (**Figure 9A**). These strains tested positive for catalase enzymes as they reduced hydrogen peroxide into water and oxygen in catalase test (**Figure 9B**). In coagulase test**,** the strains coagulated the serum samples (**Figure 9C**). Complete haemolysis in presence of these strains was found in the blood agar plates (**Figure 9D**). In the mannitol salt agar (MSA) plates, the phenol red indicator turned yellow, in presence of these strains, indicating that these are strains of *S. aureus* (**Figure 9E**). Further experiments were performed using these five identified *S. aureus* strains.

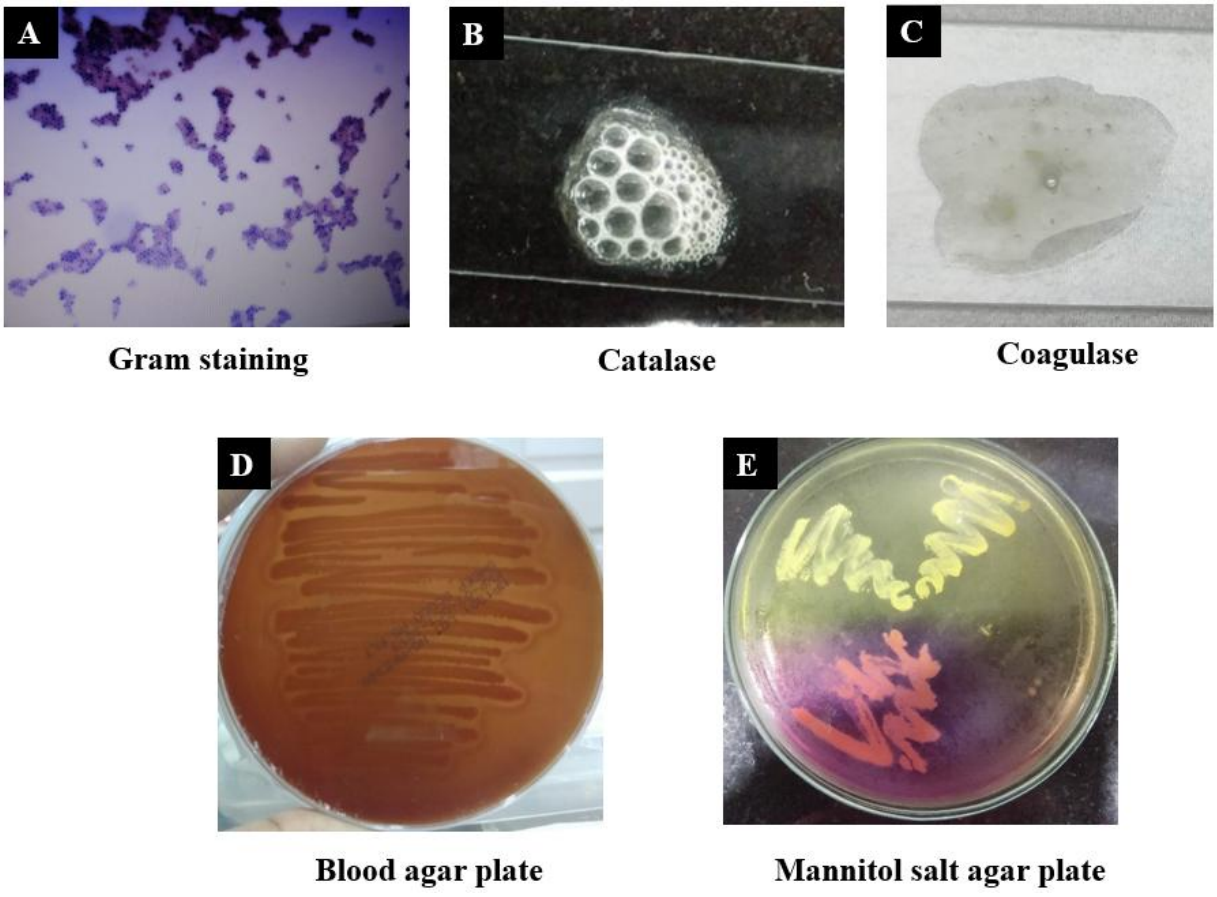

Figure 9 Results of identification of *S. aureus* by biochemical tests; **A:** Gram staining, **B:** Catalase, **C:** Coagulase, **D:** Blood agar plate, **E:** Mannitol salt agar plate.

Table 6: Biochemical test results

Sl. No.	CA *S. aureus* number	Biochemical test	Results

1.	CA 6, CA 13, CA 17, CA 21, CA 25	Gram staining, catalase, coagulase, blood agar plate, mannitol salt agar	positive

5.8.2. Genetic identification of bacterial strains

The five bacterial strains showed positive results in genetic method. 16S rDNA gene was found in agarose gel electrophoresis (**Figure 10A**) and was identified as CA 6, CA 13, CA 17, CA 21, CA 25 in NCBI (**Table 7**).

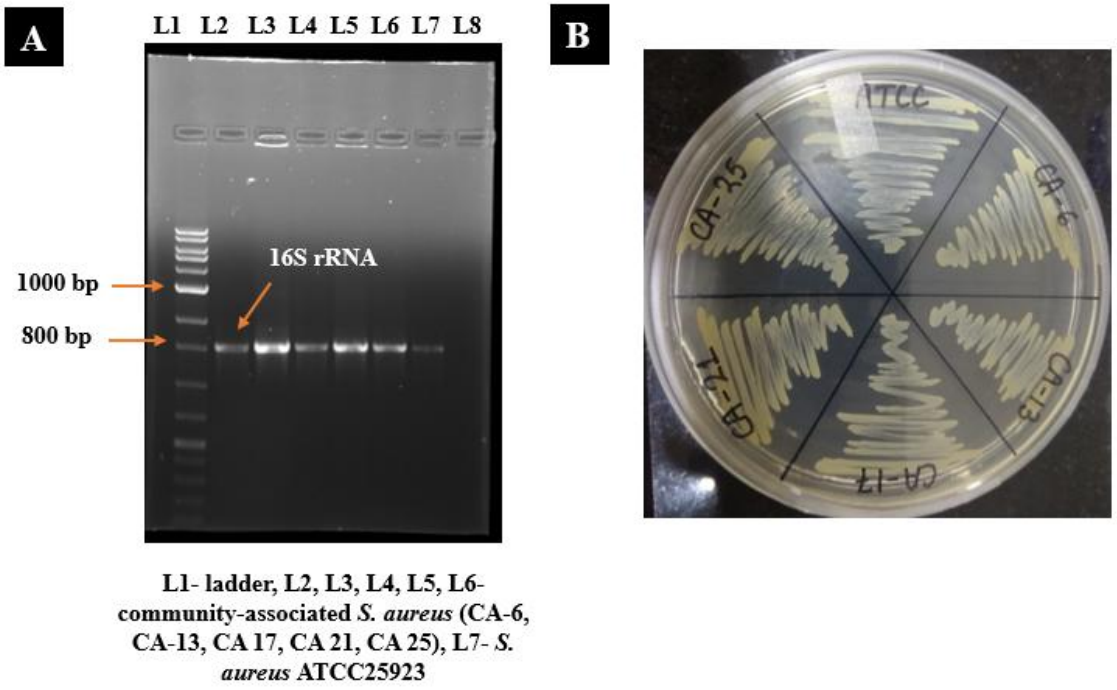

Figure 10 A: 16S rDNA gene of bacterial DNA, **B:** Collected bacterial strains on NA plate

Table 7: Collected community associated (CA) strain's name and accession number in NCBI

Sl. No.	CA *S. aureus*	Gene bank accession number
1	CA 6	OK065655.1
2	CA 13	OK065819.1
3	CA 17	OK065820.1
4	CA 21	OK065823.1
5	CA 25	MW850473.1

5.9. Phylogenetic analysis

Phylogenetic analysis showed the genetic relationship of the five CA *S. aureus* strains with another two *S. aureus* (*S. aureus* NBRC 100910 and *S. aureus* ATCC 12600) and *E. coli* (*E. coli* U 5/41). Phylogenetic analysis showed that five strains are closely related with *S. aureus* strains, belonging to the *S. aureus* family (**Figure 11**).

Staphylococcus aureus strain CA 17
Staphylococcus aureus strain CA 6
Staphylococcus aureus strain NBRC 100910
Staphylococcus aureus strain ATCC 12600
Staphylococcus aureus strain CA 13
Staphylococcus aureus strain CA 21
Staphylococcus aureus strain CA 25
Escherichia coli strain U 5/41
0.02

Figure 11 Phylogeny shows the genetic relationship of strain.

5.10. Identification of bacterial genes

Mec A, *nuc* and *pvl* gene was identified in CA and clinical *S. aureus* strains (**Figure 12**). *Mec A* gene was not found in *S. aureus* ATCC 25923 as it is a methicillin sensitive strain. *SCC mec I* and *tsst-1* gene was found only in clinical strain as it indicated the virulency of the clinical strain (**Figure 13**).

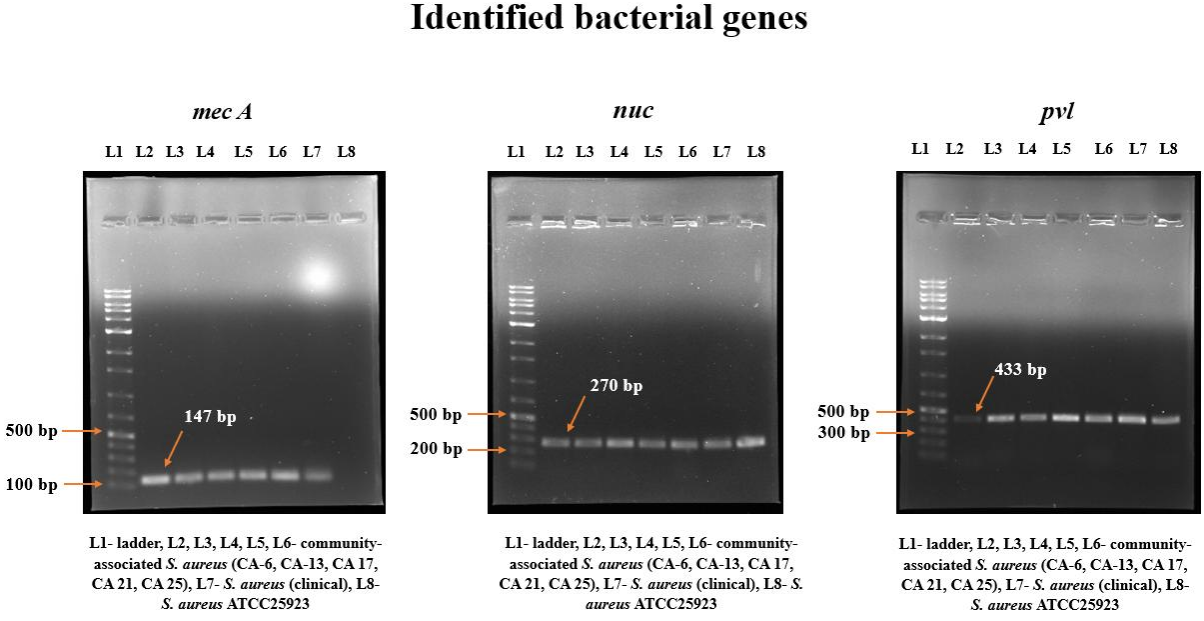
Identified bacterial genes
mec A
L1 L2 L3 L4 L5 L6 L7 L8
147 bp
500 bp
100 bp
L1- ladder, L2, L3, L4, L5, L6- community-associated S. aureus (CA-6, CA-13, CA 17, CA 21, CA 25), L7- S. aureus (clinical), L8- S. aureus ATCC25923
nuc
L1 L2 L3 L4 L5 L6 L7 L8
270 bp
500 bp
200 bp
L1- ladder, L2, L3, L4, L5, L6- community-associated S. aureus (CA-6, CA-13, CA 17, CA 21, CA 25), L7- S. aureus (clinical), L8- S. aureus ATCC25923
pvl
L1 L2 L3 L4 L5 L6 L7 L8
433 bp
500 bp
300 bp
L1- ladder, L2, L3, L4, L5, L6- community-associated S. aureus (CA-6, CA-13, CA 17, CA 21, CA 25), L7- S. aureus (clinical), L8- S. aureus ATCC25923

Figure 12 Identification of *mec A, nuc, pvl* gene of bacterial strains

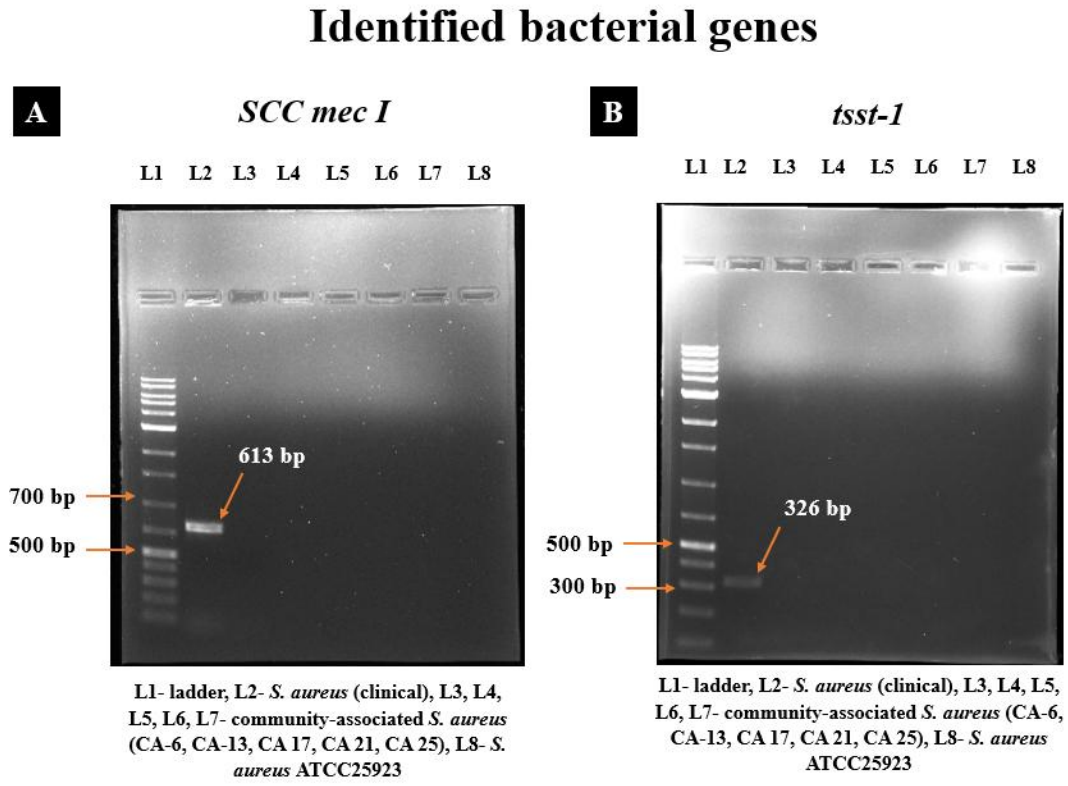
Identified bacterial genes
A
SCC mec I
L1 L2 L3 L4 L5 L6 L7 L8
613 bp
700 bp
500 bp
L1- ladder, L2- S. aureus (clinical), L3, L4, L5, L6, L7- community-associated S. aureus (CA-6, CA-13, CA 17, CA 21, CA 25), L8- S. aureus ATCC25923
B
tsst-1
L1 L2 L3 L4 L5 L6 L7 L8
326 bp
500 bp
300 bp
L1- ladder, L2- S. aureus (clinical), L3, L4, L5, L6, L7- community-associated S. aureus (CA-6, CA-13, CA 17, CA 21, CA 25), L8- S. aureus ATCC25923

Figure 13 Identification of *SCC mec I* and *tsst-1* gene of bacterial strain

5.11. Antibiotic susceptibility test

The results showed that all the strains were resistant to more than one antibiotic (**Table 8**) (**Figure 14, 15**).

Table 8: Bacterial strain resistant to antibiotics

Antibiotics	Resistant strains
AMP, AT, NX, CFM	CA 6
AMP, AT, NX, MET, CFM	CA 13
AMP, AT, NX	CA 17
AMP, AT, NX, CFM	CA 21
AMP, AT, NX	CA 25
K, AMP, AT, NX, MET, CFM	Clinical

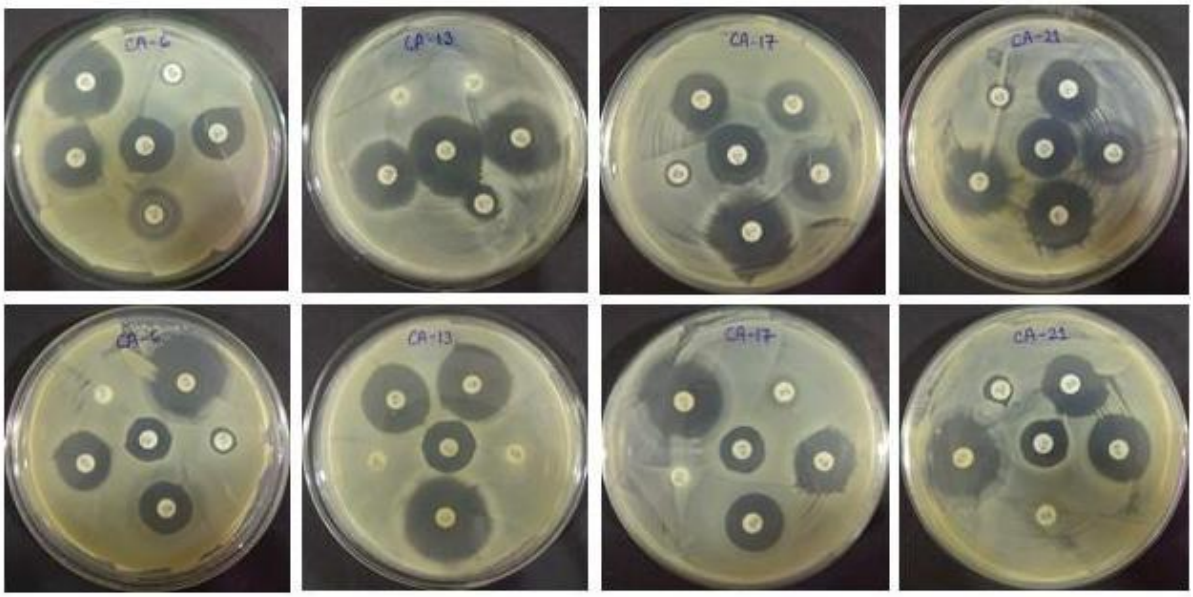

Figure 14 Antibiotic susceptibility test against the bacteria CA 6, CA 13, CA 17, CA 21

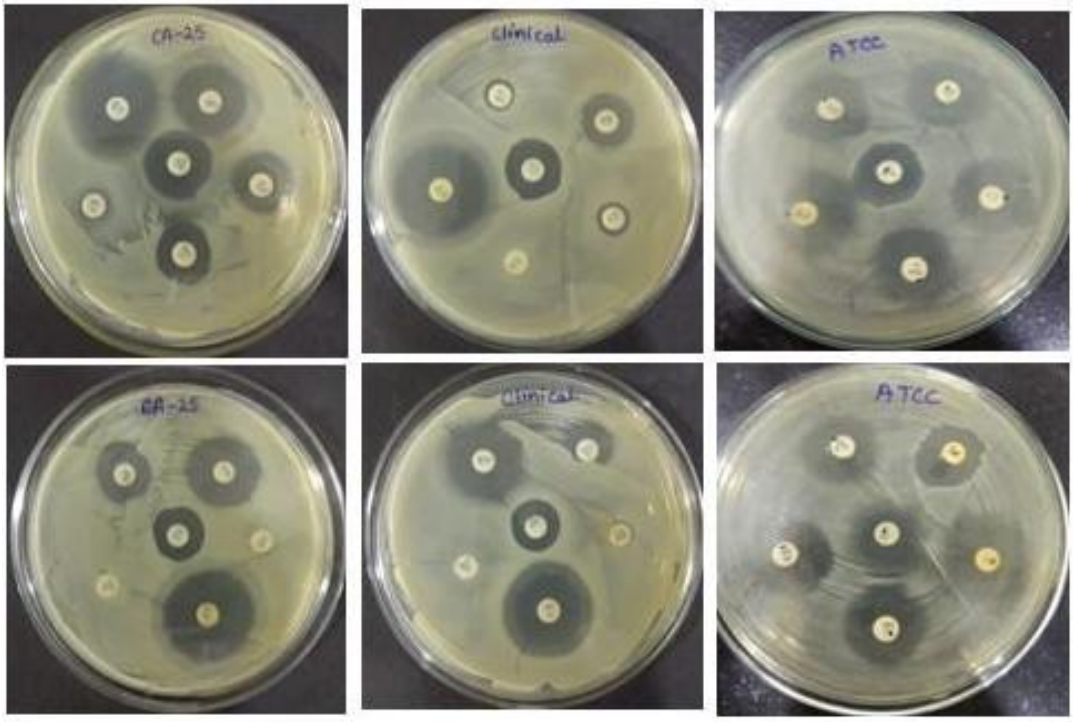

Figure 15 Antibiotic susceptibility test against the bacteria CA 25, Clinical, *S. aureus* ATCC 25923

5.12. Antimicrobial activity of AgNPs by agar well diffusion method

It is found that the synthesized NPs and vancomycin have good antibacterial activity against *S. aureus* strains and have higher antibacterial activity than the extract alone (**Figure 16**). The

highest antibacterial activity of AgNPs was found against standard strain and CA 21; and lowest antibacterial activity was found against clinical strain (**Figure 17**).

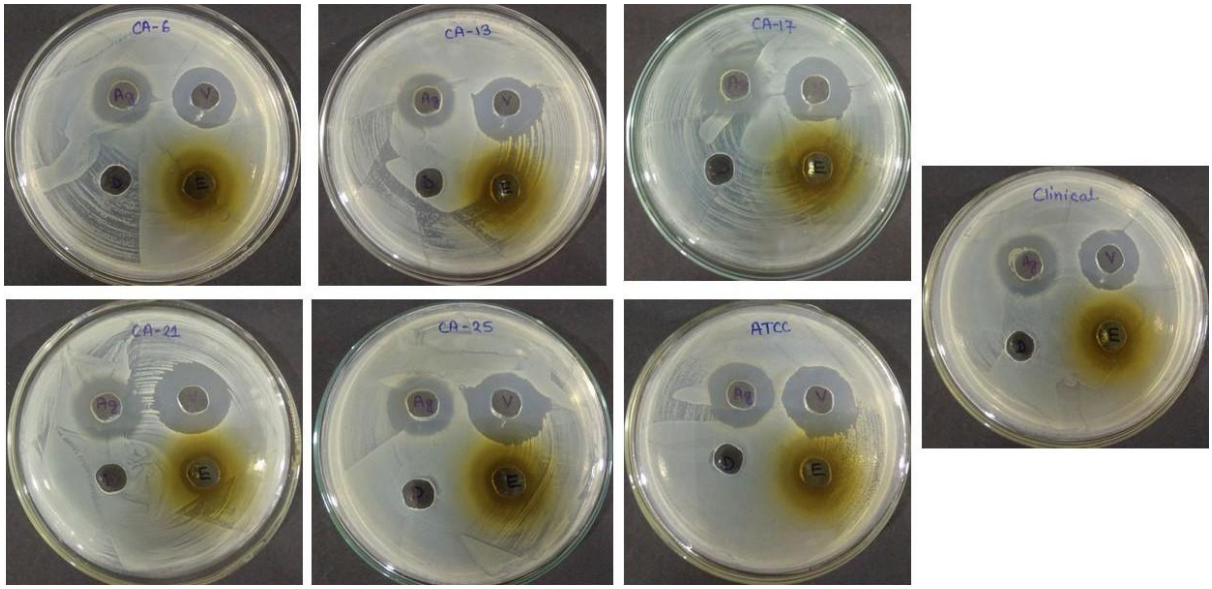

Figure 16 Antibacterial activity of AgNPs, vancomycin and extract against *S. aureus* strain. Here, Ag= AgNPs, V= Vancomycin, E= Extracts, D= Distilled water.

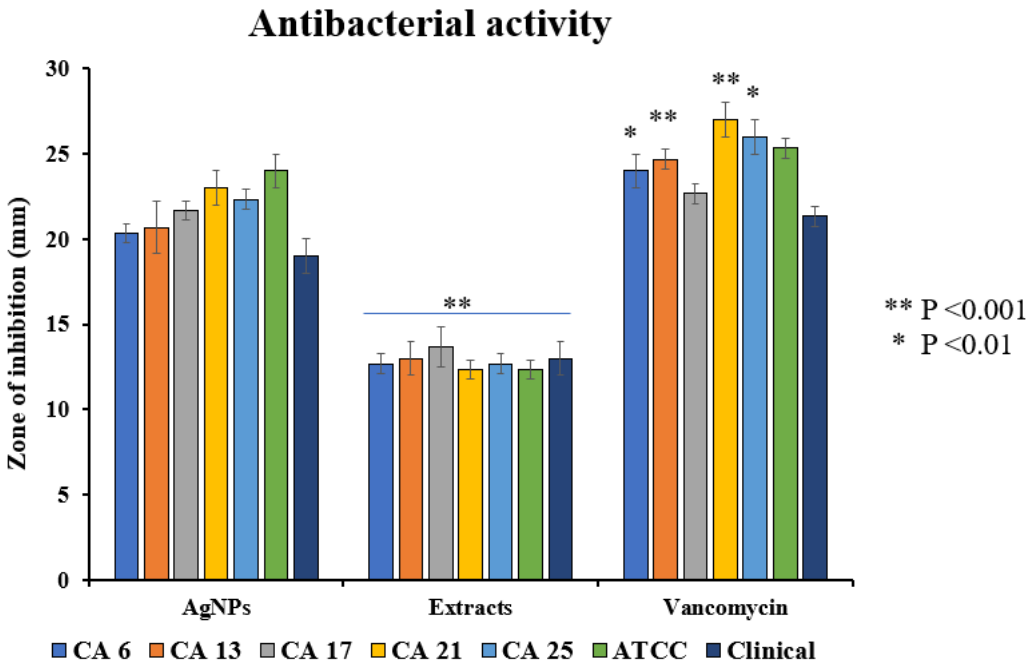

Figure 17 Graphical representation of the antibacterial activity of AgNPs, extract and vancomycin. Significance level one-way ANOVA [*p<0.05, **p<0.01, ***p<0.001, NS: No significant difference.

5.13. Results of quantitative study

Minimum bactericidal effects against community associated and standard bacterial strains were exhibited with various degrees in AgNPs (**Figure 18**). The MIC and MBC values of green synthesized AgNPs against *S. aureus* strains ranged from 15.62 to 31.25 µg/mL (**Figure 19**).

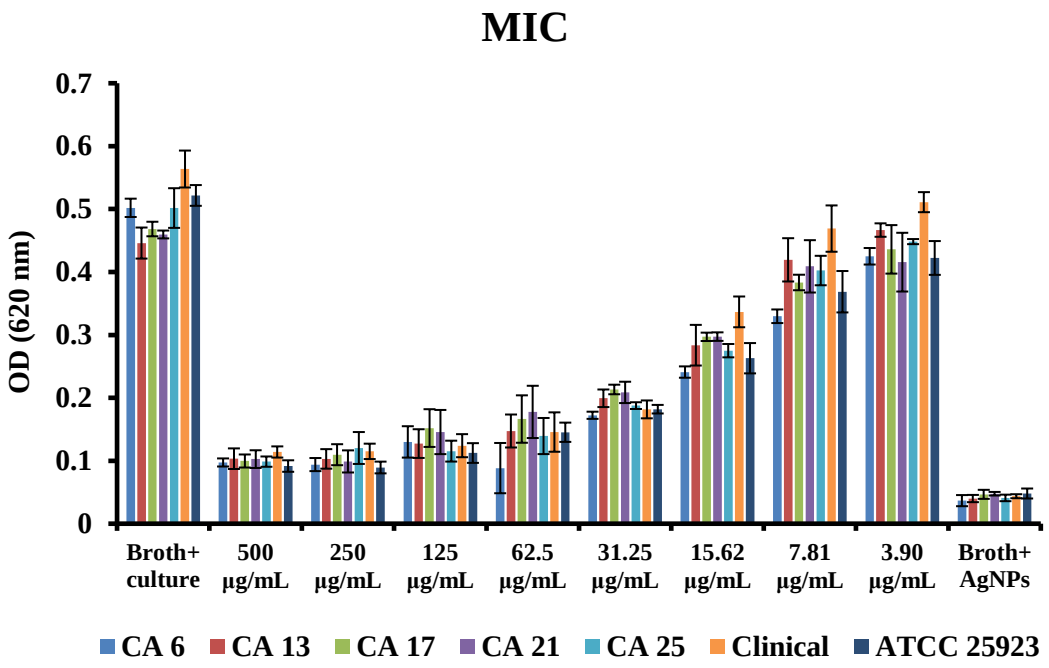

Figure 18 MIC and MBC study of AgNPs in microtiter plate

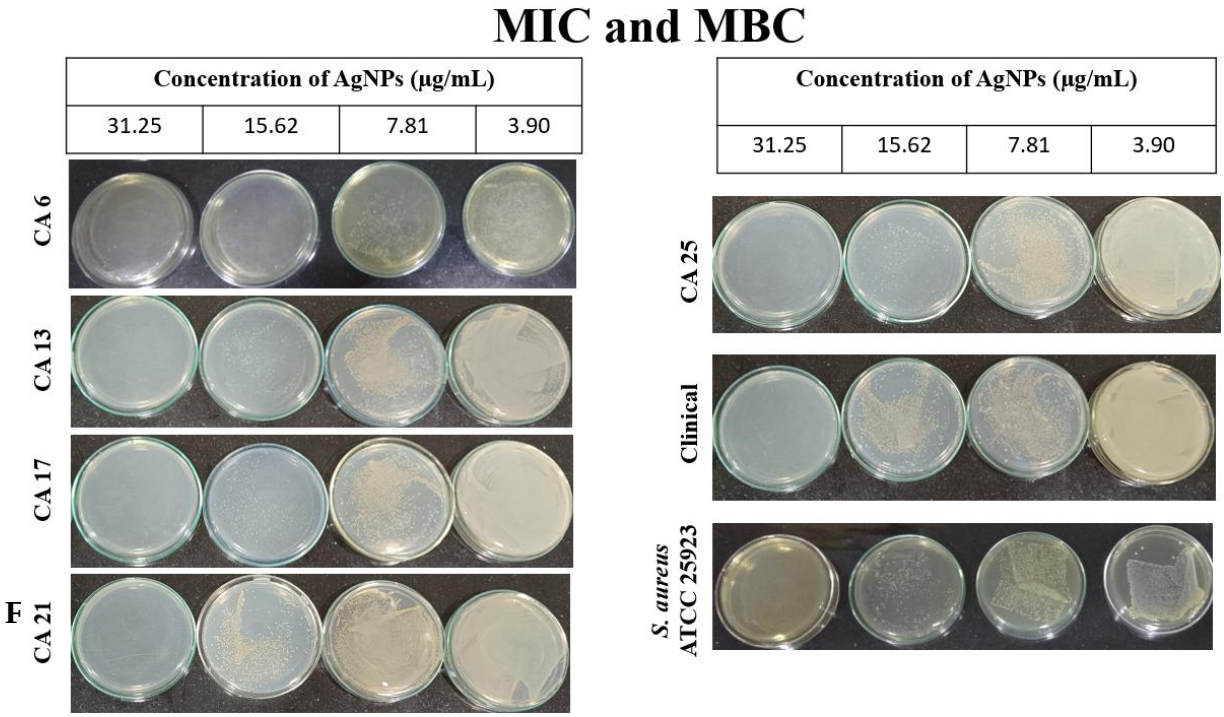

5.14. Effect of AgNPs on growth curve

In this study, the growth of *S. aureus* was observed in different phases without AgNPs treatment and three phases were identified as lag, exponential and late-exponential-to-stationary. The impact of AgNPs on *S. aureus* growth was then investigated. During the lag phase, MIC concentration inhibited *S. aureus* growth which leads to complete inhibition. However, at sub-MIC concentration, *S. aureus* persisted in the exponential phase of bacterial growth (**Figure 20**).

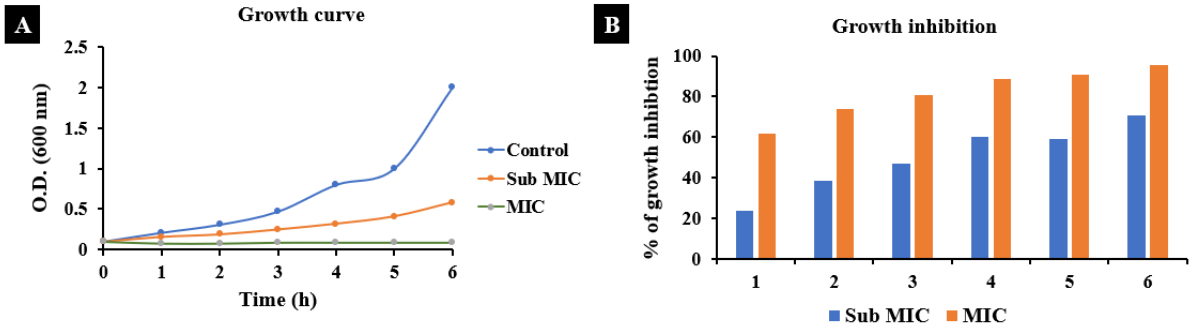

Figure 20 A. Impact of AgNPs on the growth curve. **B.** Percentage of growth inhibition revealed notable effects, with the MIC-treated group exhibiting 95.5% inhibition and in case of sub-MIC treated group 71% growth inhibition was observed.

5.15. Bacterial cell membrane damage

Noticeable alterations in cell membrane morphology were observed over the treatment period. After 6 hours, damage, creases and fragments were evident on the cell membrane, attributed to NP attachment. In contrast, the control group of *S. aureus* cells (**Figure 21**) maintained their characteristic grape-like cluster shape with an intact surface and no observable damage was found.

Mag=10000x **Mag=25000x**

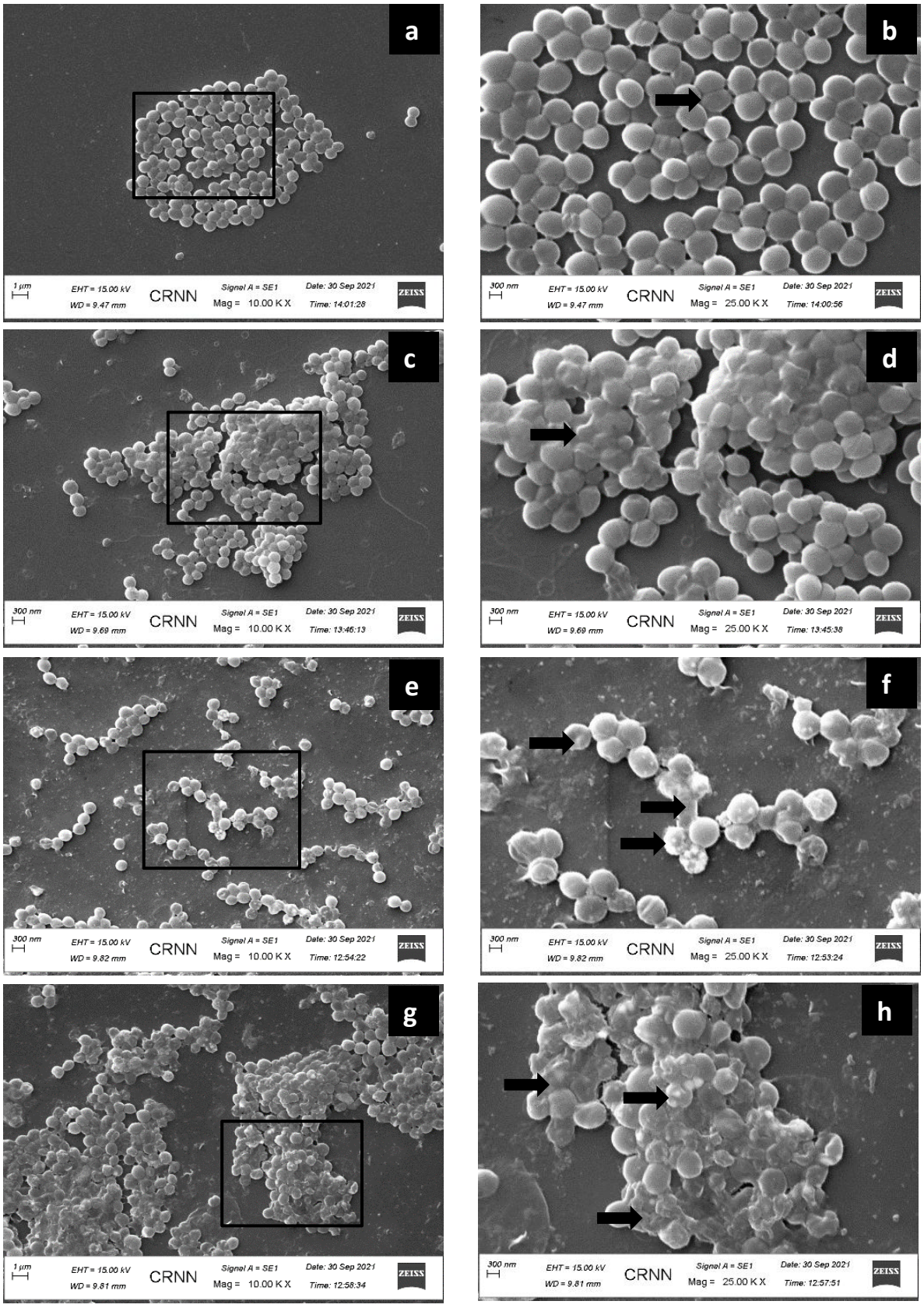

Figure 21 SEM observations depicting morphological alterations in *S. aureus* cells subjected to AgNPs treatment for varying durations under different magnifications of 10000x and 25000x. **(a, b):** Control images display an intact bacterial membrane for untreated bacteria. **(c, d):** *S. aureus* cells treated with AgNPs for 2 hours exhibit cell clumping, indicative of bacterial membrane damage. **(e, f):** After 4 hours of AgNPs treatment, *S. aureus* cells display irregular shapes and wrinkles. **(g, h):** A 6-hour treatment with AgNPs results in prominent damage, wrinkles and fragmentary pieces of the cell membrane. Black arrows highlight changes in bacterial cell membranes. Images **(a, c, e, g)** are SEM images observed at 10000x, while images **(b, d, f, h)** are SEM images observed at a magnification of 25000x.

5.16. Bacterial surface morphology study using AFM

The **Figure 22** displays both 2D and corresponding 3D reconstruction images of *S. aureus* following treatment with AgNPs. In the control group, the bacterial surface appeared smooth. However, in the AgNPs-treated group, cell borders became rough, indistinct, indicating the presence of extracellular slime and exhibited notable distortions in morphology. However, in the untreated control group, no noteworthy alterations in cell dimensions were observed.

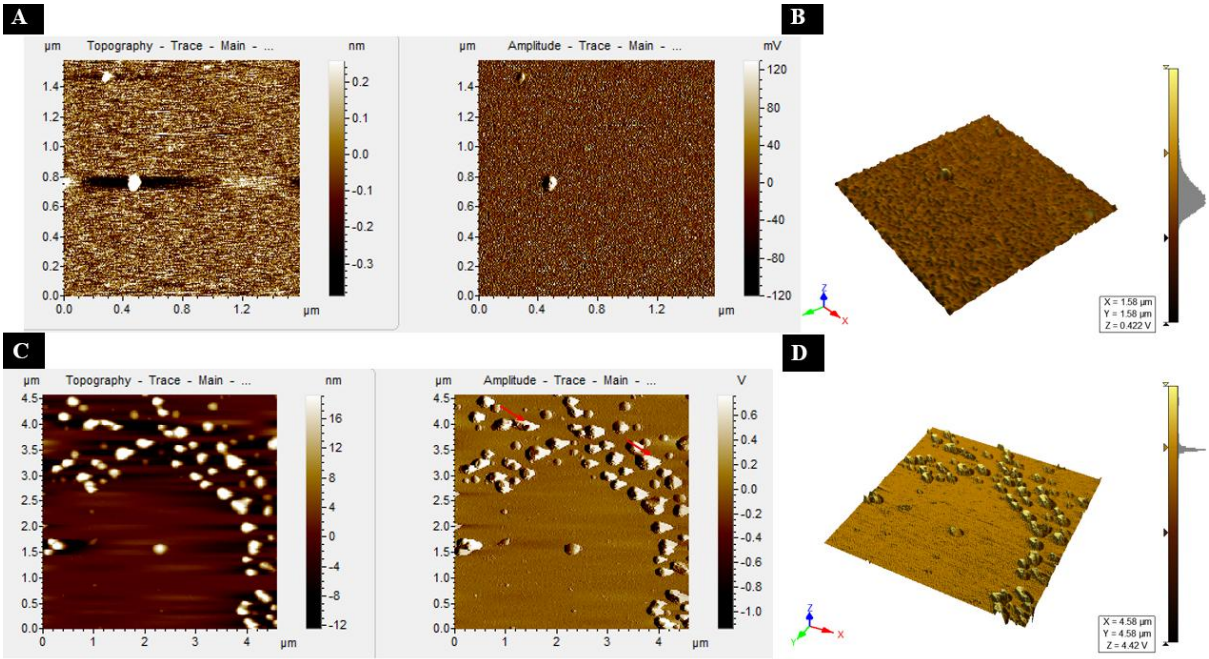

Figure 22 Morphological analysis of *S. aureus* under AFM, **A:** Control: Two-dimensional topography and amplitude image of *S. aureus* without any treatment (control), **B:** three-dimensional image of the same *S. aureus* without any treatment (control), **C:** Two-dimensional topography and amplitude image of *S. aureus* treated with 31.25 µg/mL (MIC value) of AgNPs

treatment, red arrow indicates bacterial cell membrane damage; **D:** Three-dimensional image of the same *S. aureus* treated with 31.25 µg/mL of AgNPs treatment.

5.17. Fluorescence microscopy (demonstration of live and dead bacterial cells)

In **Figure 23**, green fluorescence indicates live cells and red fluorescence signifies dead cells. The study found that AgNPs caused damage to the bacterial membrane, leading to cell death (red fluorescence). Image analysis (**Figure 24**) showed higher green fluorescence intensity in the control and higher red fluorescence intensity in dead bacteria.

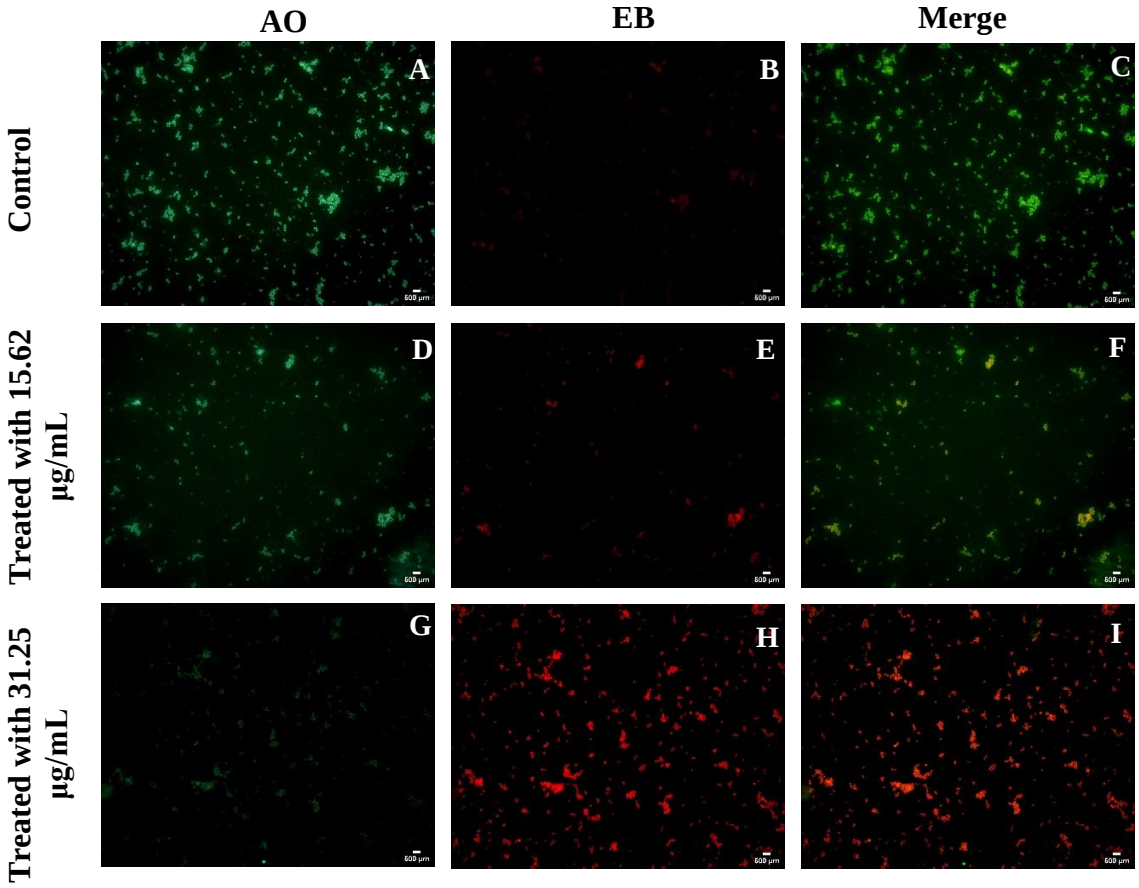

Figure 23 Fluorescent microscopy observations of *S. aureus* exposed to AgNPs. Control images (**A, B, C**) reveal higher green fluorescence, indicating the presence of live bacteria. Treatment with sub-MIC concentration of AgNPs (**D, E, F**) exhibits higher green fluorescence than red, indicating a higher proportion of live cells compared to dead cells. Treatment with MIC concentration of AgNPs (**G, H, I**) displays higher red fluorescence than green, indicating a higher presence of dead cells.

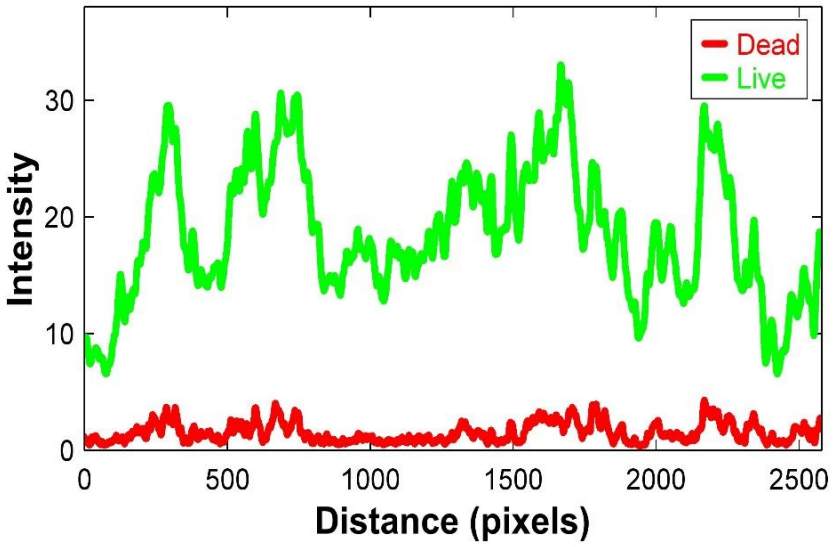

RGB profile of the merged image of the control

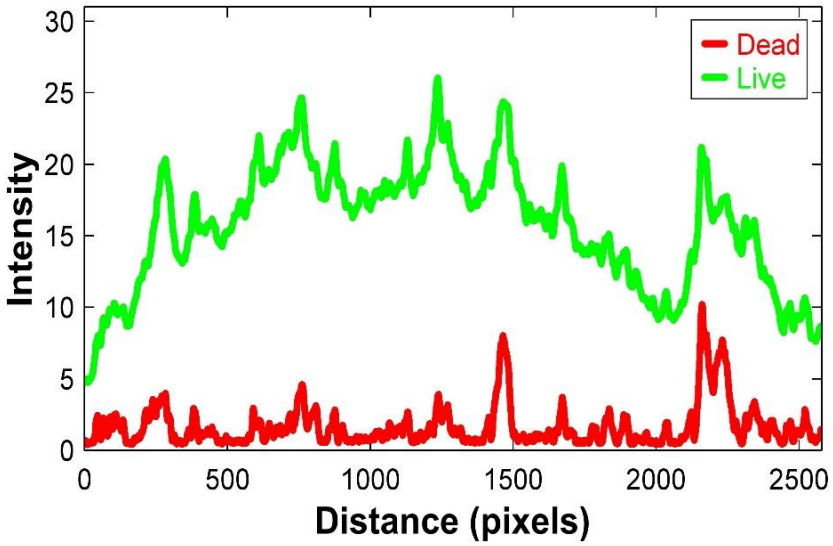

RGB profile of merged image of bacteria treated with 15.62 µg/mL of AgNPs (1/2 MIC)

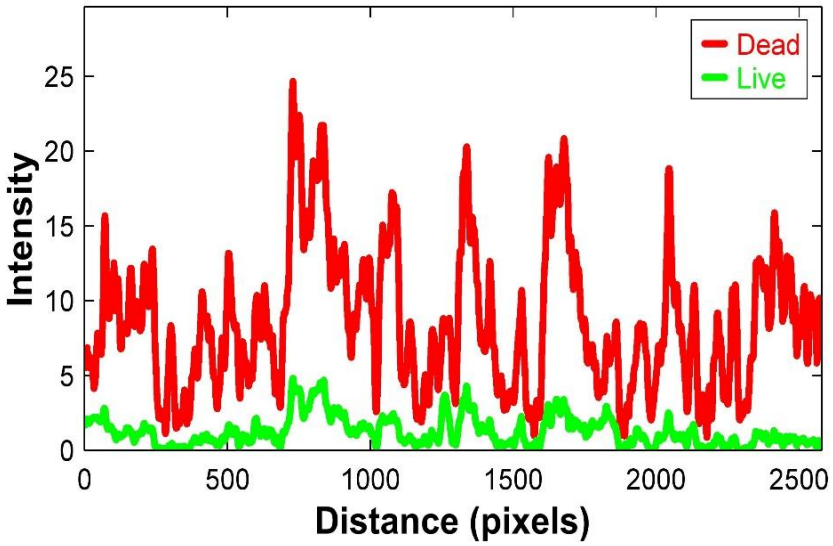

RGB profile of merge image of bacteria treated with 31.25 µg/mL of AgNPs (MIC)

Figure 24 RGB profile of merged images of bacterial cells

5.18. Single-cell gel electrophoresis (comet assay)

Comet tails, indicating bacterial DNA damage, were observed after 2 hours of treatment with each antimicrobial agent. The negative control (untreated) remained intact in the comet assay (**Figure 25**). The comet assay revealed significant DNA damage in each treated case, as evidenced by statistically significant head movement, tail movement and olive tail movement compared to the control group (**Figure 26**).

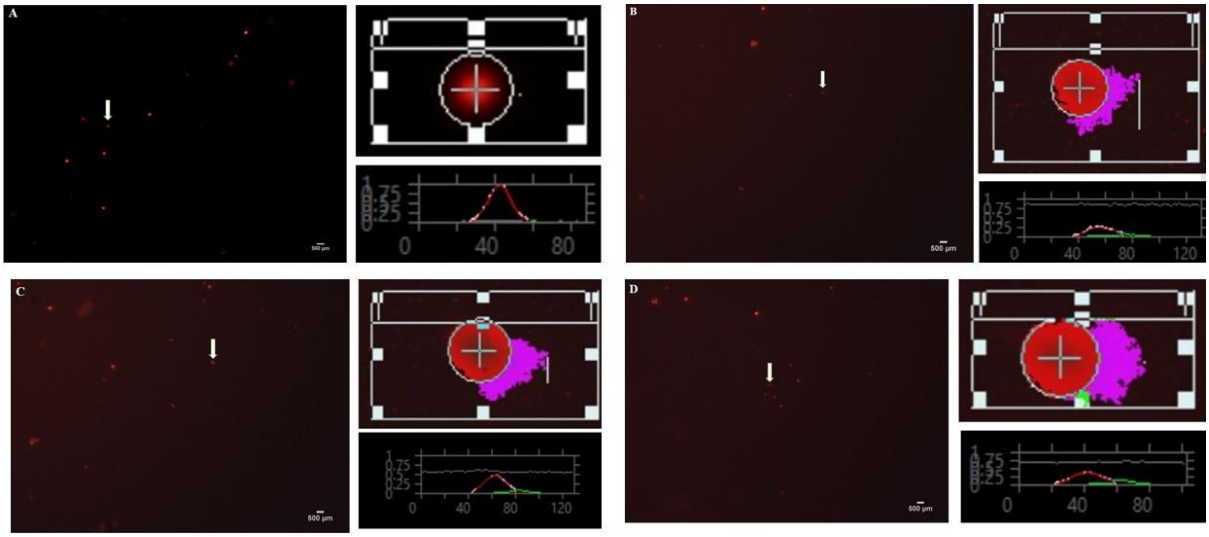

Figure 25 Results of single-cell gel electrophoresis (comet assay), **A.** Control: No DNA migration in the undamaged cell, **B.** AgNPs treated: Mild increase in DNA migration to the tail, **C.** VCN treated: Mild increase in DNA migration to the tail, **D.** VNPs treated: Moderate increase in DNA migration.

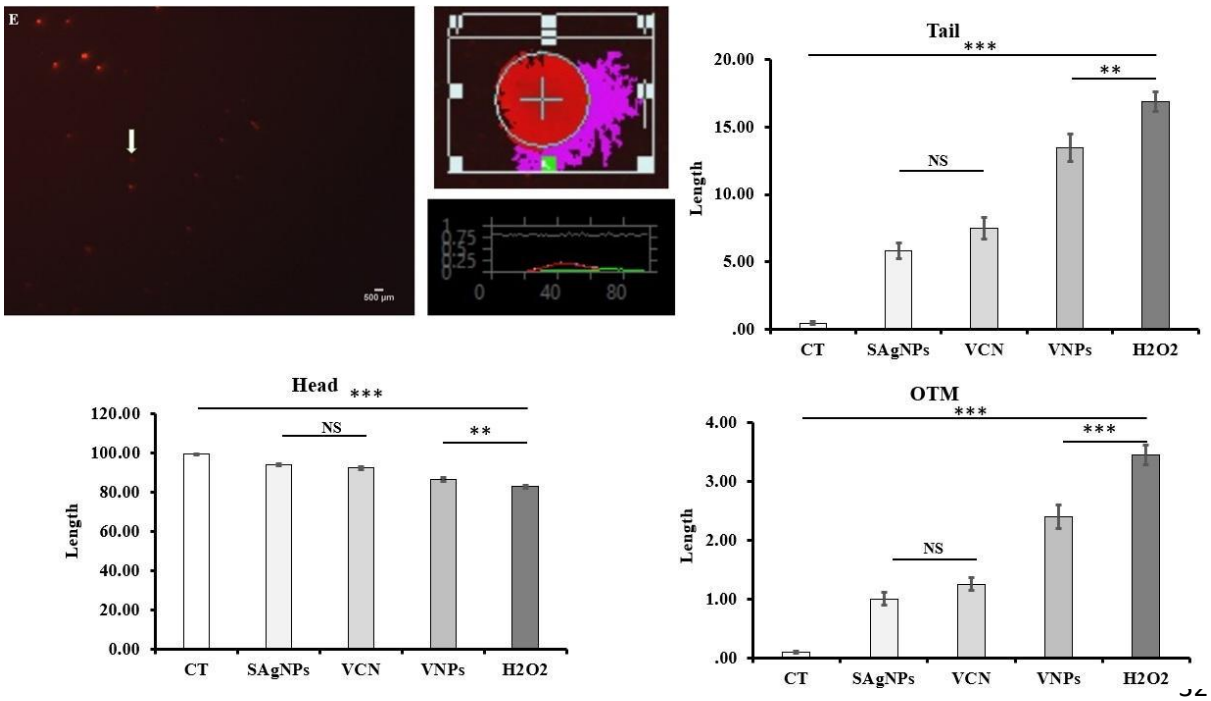

Figure 26 Results of Single-cell gel electrophoresis (comet assay), **E.** H_2O_2 treated: Moderate increase in DNA migration, **F.** Tail movement, **G.** Head movement, **H.** Olive tail movement. Significance level one-way ANOVA, Tukey test [*p<0.05, **p<0.01, ***p<0.001, NS: No significant difference.

5.19. Quantification of bacterial death using FACS

PI staining revealed that 67.5% of *S. aureus* cells were nonviable when treated with the MIC concentration of AgNPs, whereas 24.8% of *S. aureus* cells were nonviable with the sub-MIC concentration of AgNPs (**Figure 28**). The highest fluorescent intensity was observed in the case of bacteria treated with the MIC. Notably, in the control groups consisting of only buffer and unstained live bacterial cells, no fluorescent intensity was detected, indicating the absence of PI-stained cells. Conversely, live cells stained with PI exhibited some fluorescent intensity, underscoring the presence of unstained viable cells (**Figure 27**).

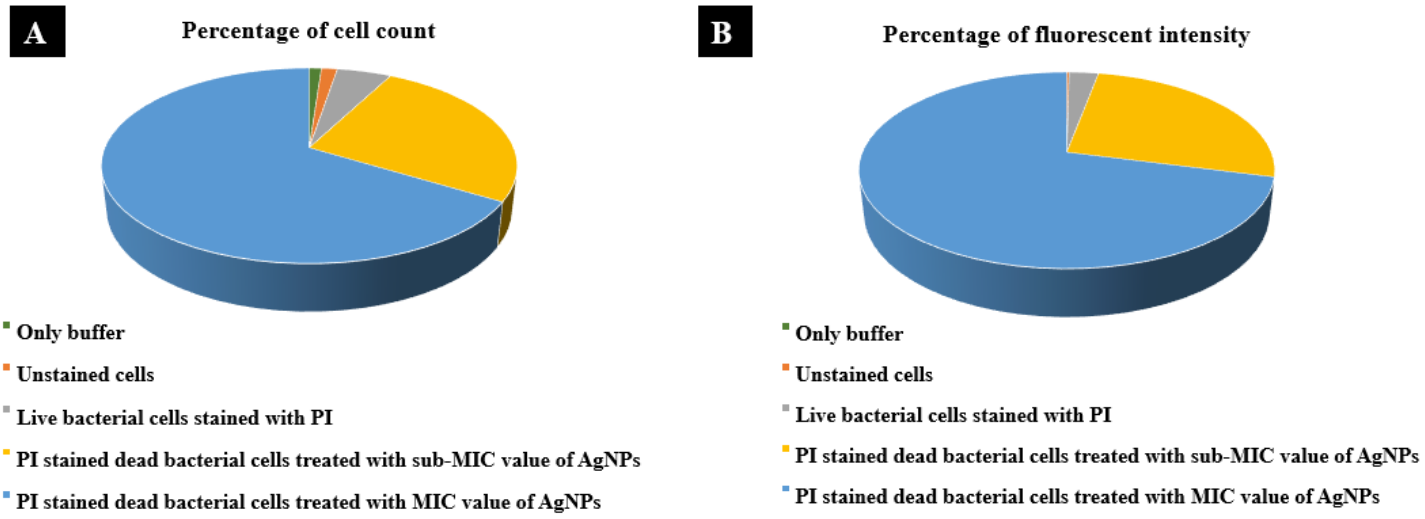
A
Percentage of cell count
Only buffer
Unstained cells
Live bacterial cells stained with PI
PI stained dead bacterial cells treated with sub-MIC value of AgNPs
PI stained dead bacterial cells treated with MIC value of AgNPs
B
Percentage of fluorescent intensity
Only buffer
Unstained cells
Live bacterial cells stained with PI
PI stained dead bacterial cells treated with sub-MIC value of AgNPs
PI stained dead bacterial cells treated with MIC value of AgNPs

Figure 27 A: Percentage of cell count of dead cells in different conditions which is illustrated in different color in the pie chart, **B:** Percentage of fluorescent intensity of dead cells in different conditions which is illustrated in different color in the pie chart. The blue color indicates more dead cells when treated with MIC concentration of AgNPs, the yellow color indicates less dead cells when treated with sub-MIC concentration of AgNPs, the grey color indicates dead bacterial cells in live cells.

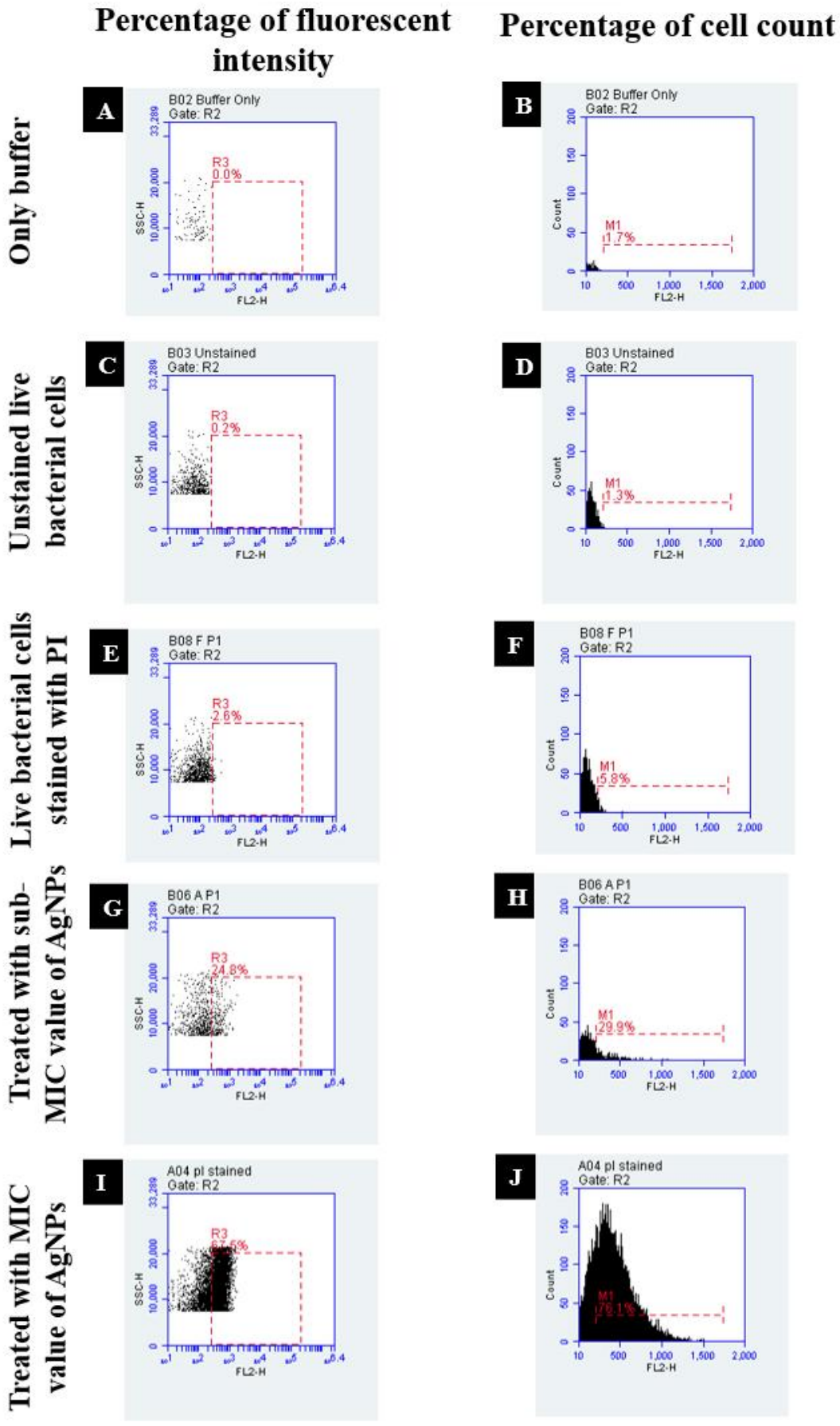

Figure 28 Percentage of fluorescent intensity and percentage of cell count of bacterial dead

cells in FACS; **A, B:** Only buffer; **C, D:** Unstained live bacterial cells; **E, F:** Live bacterial cells stained with PI; **G, H:** Treated with sub-MIC concentration of AgNPs; **I, J:** Treated with MIC value of AgNPs.

5.20. Photocatalytic degradation

The study identified a distinctive absorption peak for MG at 617 nm (**Figure 29A**). A time-dependent decrease in absorption was found in the presence of 0.5 mg/mL AgNPs, a remarkable 97.21% degradation occurred in 90 minutes (**Figure 29B**), changing the colour of the solution from dark blue to light blue. The degradation rate was 0.034±0.005 min^{-1} (**Figure 29C**).

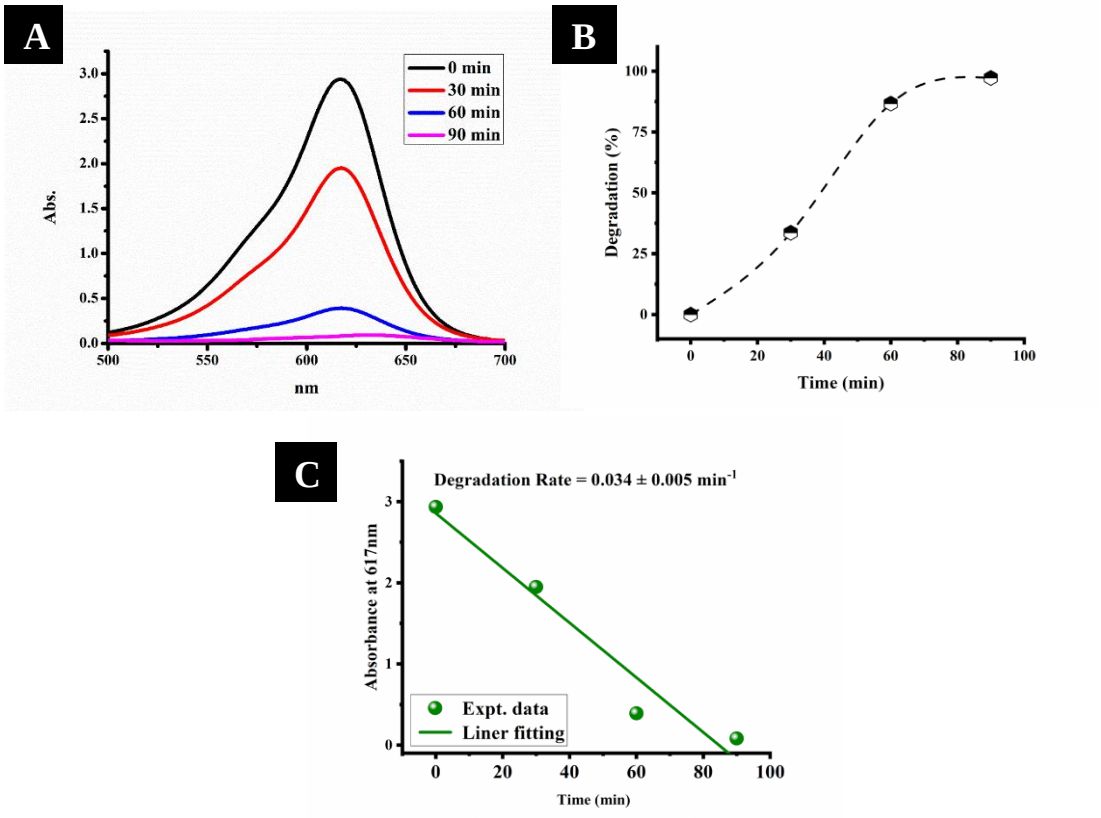

Figure 29 Photocatalytic degradation of MG facilitated by AgNPs under sunlight irradiation. **A:** UV-Visible spectra depict the photocatalytic degradation for varying exposure times. **B:** The percentage of degradation is presented over the exposure time. **C:** The rate of degradation of MG dye in the presence of AgNPs is determined to be 0.034±0.005 min^{-1} under sunlight exposure.

5.21. Bacterial load in animal model

Counting the bacterial load of the knee joint showed a huge number of bacterial colonies in the arthritis control groups (**Figure 30**). The bacterial load was uncountable in case of arthritis control group and a reduction of bacterial load was observed in NPs, vancomycin and in combinedly treated groups on day 14 (**Table 9**). A notable distinction was observed in the group treated with a combination, as compared to the other treatment groups.

Table 9: Number of bacterial colonies in different groups

Groups	Bacterial colonies
Normal control (NC)	Not detectable
Only AgNPs treated (NP)	Not detectable
Arthritis control (AC)	Uncountable
AgNPs treated group (TNPs)	5625.00 ± 419.92
Vancomycin treated group (VCM)	4750.0000 ± 313.39
AgNPs and vancomycin treated group (VNP)	1125.00 ± 226.58

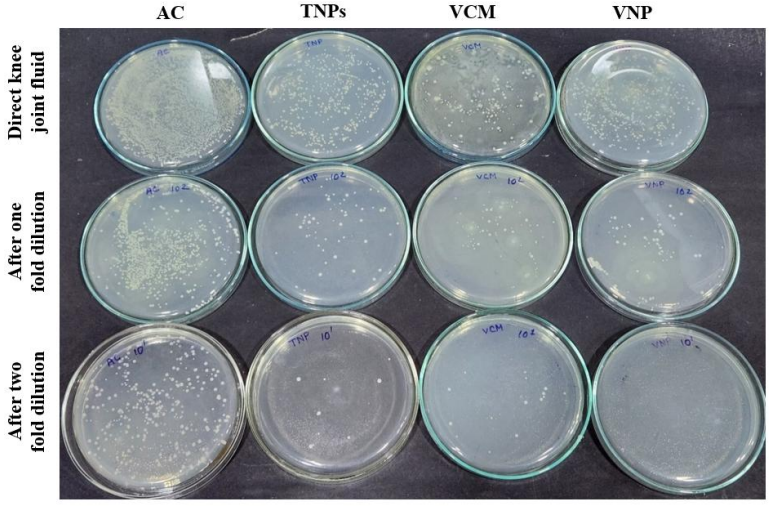

Figure 30 Bacterial colonies after two-fold dilution of knee joint fluid; **AC:** Arthritis control; **TNPs:** NPs treated group; **VCM:** Vancomycin treated group; **VCM:** NPs and vancomycin treated group.

5.22. Animal weight

All bodyweight data recorded over day 0, 7 and 14 days of the experiment showed significant differences between treatment groups in comparison with the AC group. The AC group and TNPs treated group had lower body weights compared to the NC (**Figure 31A**).

5.23. Organ index

No significant differences were found between the treatment groups and controls from day 0 to day 14 (**Figure 31B**).

5.24. Knee joint diameter

After day 14, a significant difference was found in case of the AC and NC group. The present study also found a significant difference in case of the treatment group in comparison to the AC group (**Figure 31C**).

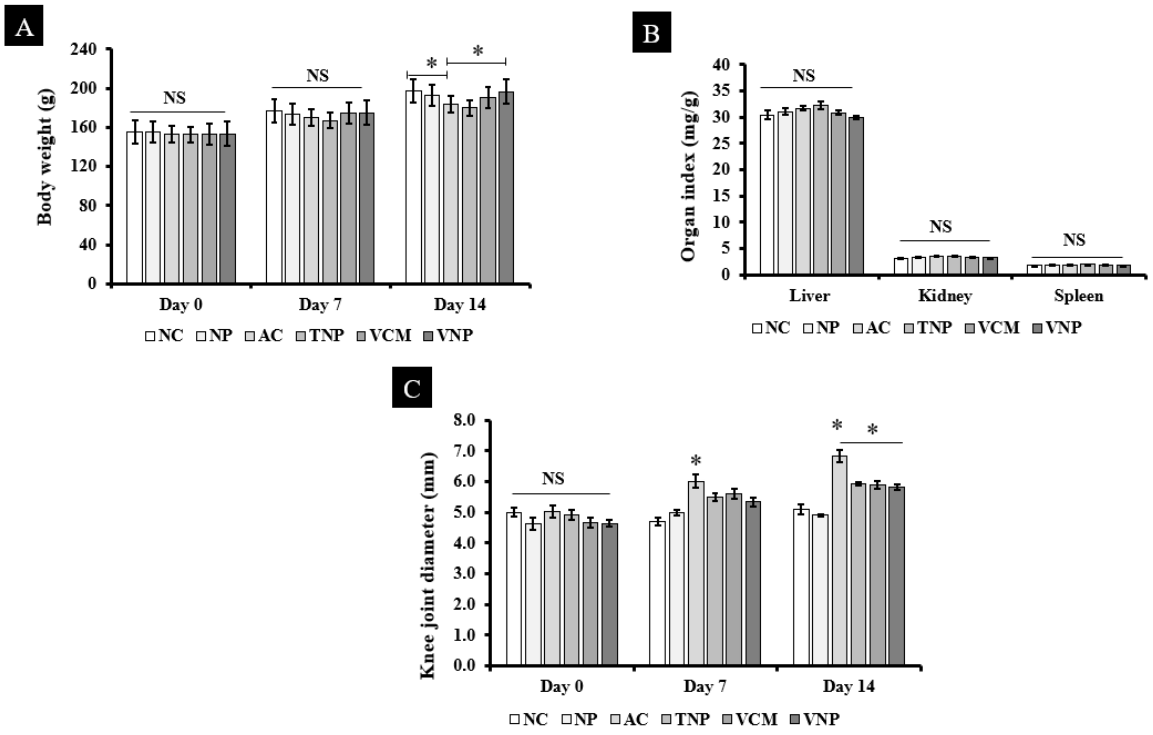

Figure 31 Impact of AgNPs and vancomycin on *S. aureus* infected male Wistar rat. **A.** body weight, **B.** organ index, **C.** knee joint diameter (mm). NC = Normal control, NP = Only nanoparticles, AC = Arthritis control, TNP = Treated with AgNPs, VCM = Treated with vancomycin, VNP = Treated with AgNPs and vancomycin. NS= No significant difference, * $p< 0.05$, ** $p<0.01$, *** $p<0.001$ compared to the AC group.

5.25. Morphological analysis of knee joint

The arthritis control (AC) group showed an inability to bend the knee joint. Examination of the knee joint of the AC group revealed surface damage and swelling of the joint tissue compare to the normal group (NC) [42]. Pus was also found in the AC group. The other groups including the NC group showed the smooth and moist knee cavity (**Figure 32**) [43].

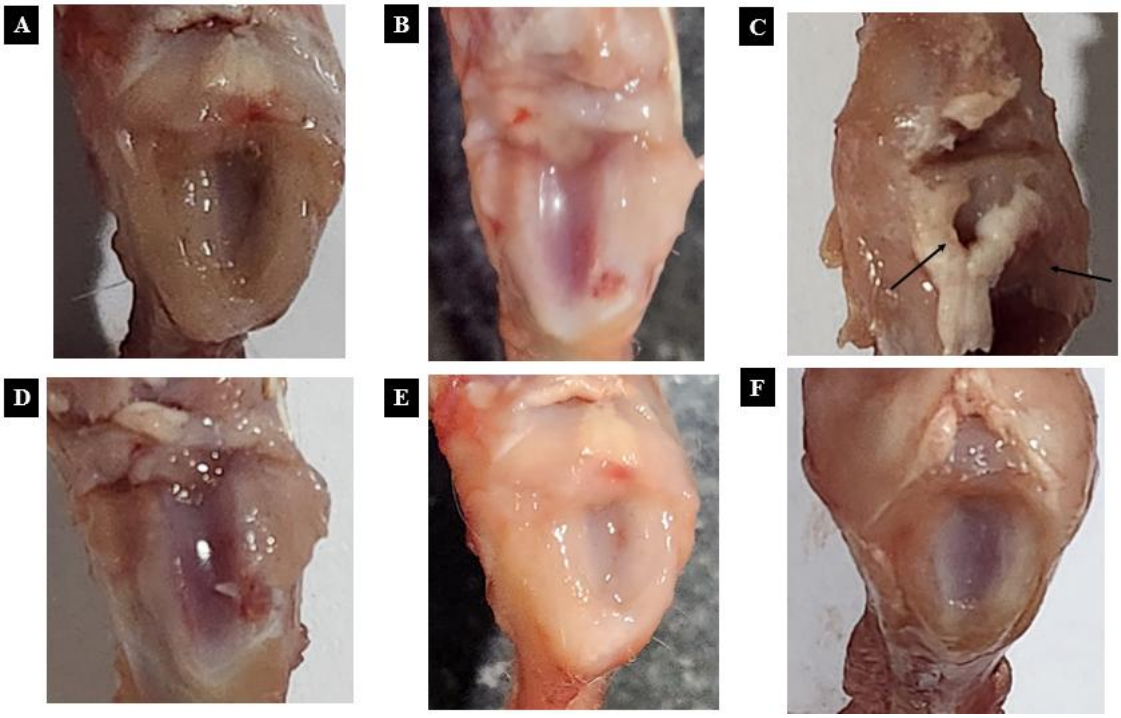

Figure 32 Morphological analysis of knee joint. **A.** Control: Normal smooth and moist knee cavity, **B.** Only AgNPs treated group, **C.** Arthritis control: Black arrow indicates swelling of tissues, **D.** NPs treated group, **E.** Vancomycin treated group, **F.** AgNPs and vancomycin treated group.

5.26. Blood parameters

Considering the number of WBC, neutrophils, lymphocytes a significant difference was found in the AC group in comparison with the NC group which indicates inflammation. A significant decrease of blood cells was found in treatment groups in comparison with the AC group. It was also found that there is no significant difference between the NC group and combinedly treated group (VNP) in case of WBC and neutrophil. This decrease of blood cells indicated the reduction of inflammation. Where in case of RBC cells there is no significant difference between the NC group and treatment groups (**Figure 33**).

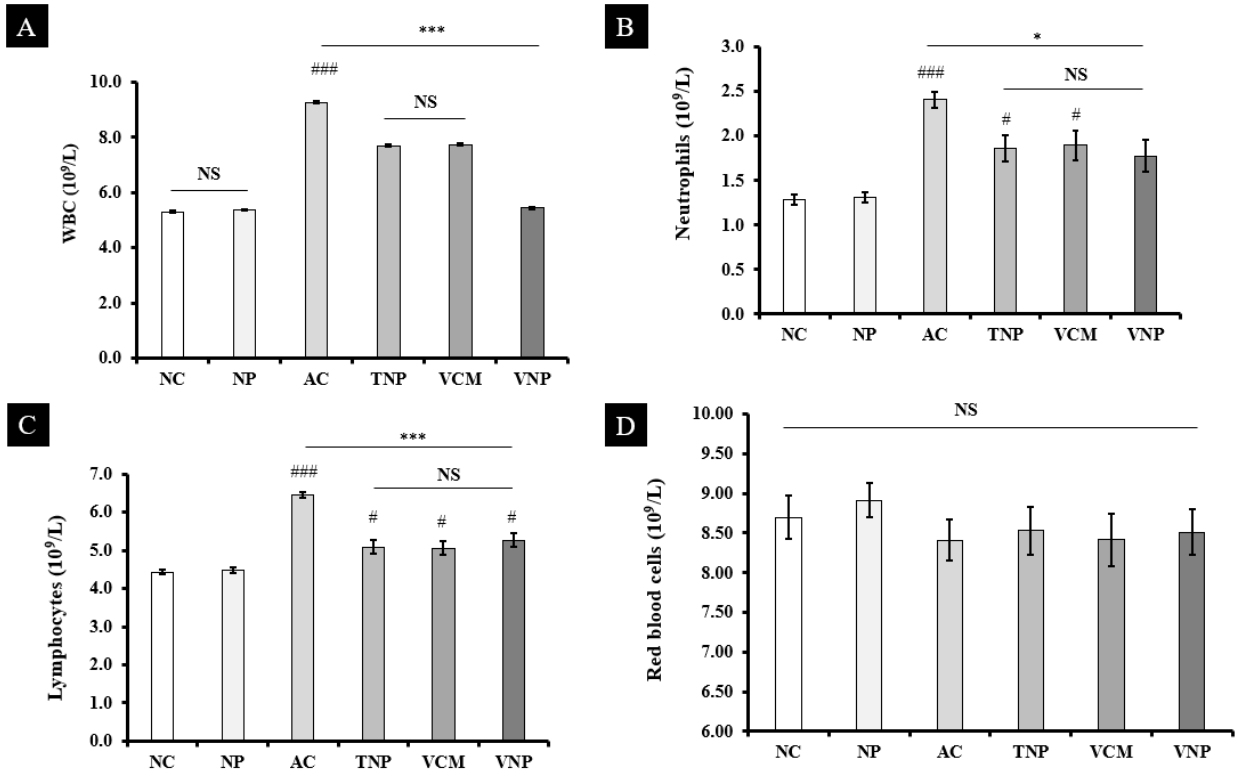

Figure 33 Impact of AgNPs and vancomycin on *S. aureus* infected male Wistar rat. **A.** WBC count, **B.** Neutrophil, **C.** Lymphocytes, **D.** RBC count. NC = Normal control, NP = Only nanoparticles, AC = Arthritis control, TNP = Treated with AgNPs, VCM = Treated with vancomycin, VNP = Treated with AgNPs and vancomycin. # $p< 0.05$, ## $p<0.01$, ### $p<0.001$ compared to the NC group; * $p<0.05$, ** $p< 0.01$, ***$p< 0.001$ compared to the AC group, NS= No significant difference.

5.27. Biochemical findings

The results of the examination of AST and ALT levels showed a significant rise in serum AST and ALT levels in the treatment group in comparison with the NC group. However, there was a significant difference in the ALT and AST levels between the AC group with the treatment groups which indicated better recovery (**Figure 34A and 34B**). Creatinine levels increased in the case of the AC as shown in **Figure 34C** and a significant decrease was found in the case of the treatment group. No significant difference was found between the NC and NP group. The concentration of total protein exhibited a notable increase in the AC group compared to the NC group. However, in the treatment groups, comprising AgNPs, vancomycin and a combination of AgNPs and vancomycin, there was a significant decrease in the protein levels (**Figure 34D**).

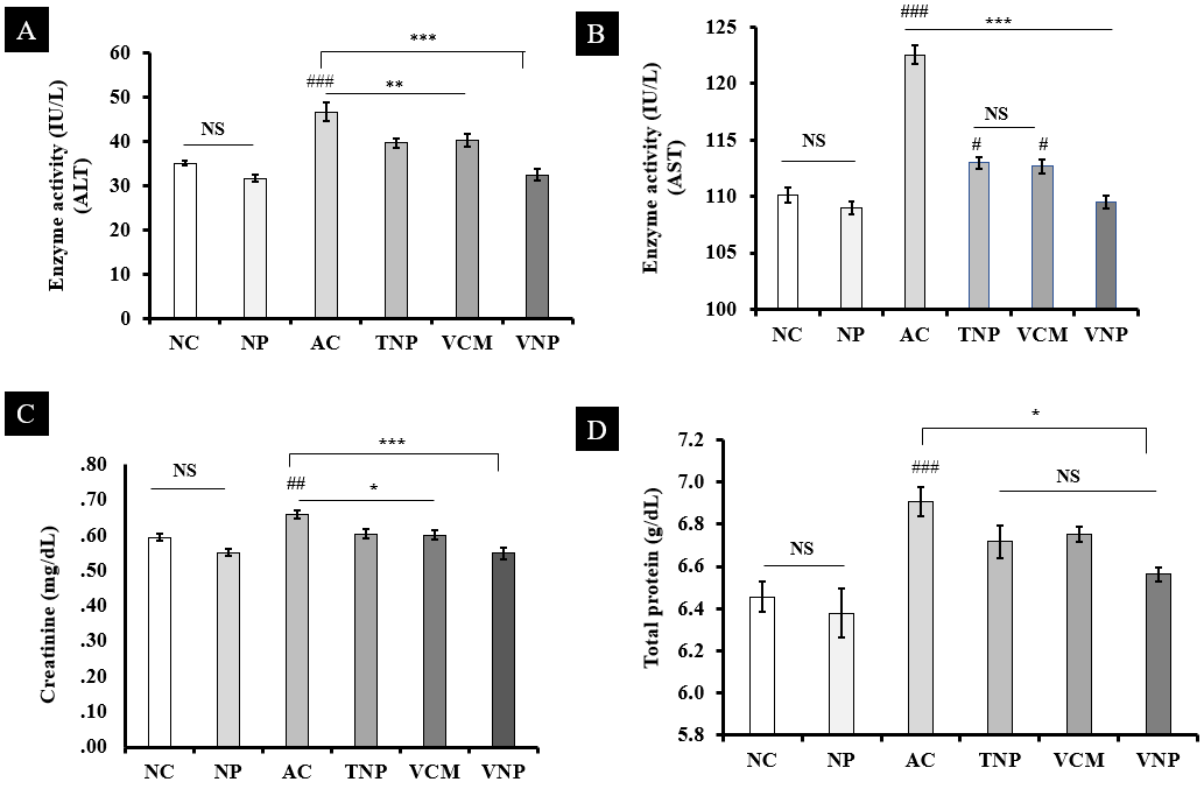

Figure 34 Impact of AgNPs and vancomycin on *S. aureus* infected male Wistar rat. **A.** ALT, **B.** AST, **C.** Creatinine, **D.** Total protein. NC = Normal control, NP = Only nanoparticles, AC = Arthritis control, TNP = Treated with AgNPs, VCM = Treated with vancomycin, VNP = Treated with AgNPs and vancomycin. # p< 0.05, ## p<0.01, ### p<0.001 compared to the NC group; * p<0.05, ** p< 0.01, ***p< 0.001 compared to the AC group, NS= No significant difference.

5.28. Effect on inflammatory marker

Rat serum inflammatory factor, IL-6 and CRP content increases in the AC group on day 14 and decreases in the treatment group (**Figure 35**). These results demonstrated that AgNPs and VCM therapy were more effective in combined form in attenuating septic arthritis as it showed less inflammation in comparison with the AC group.

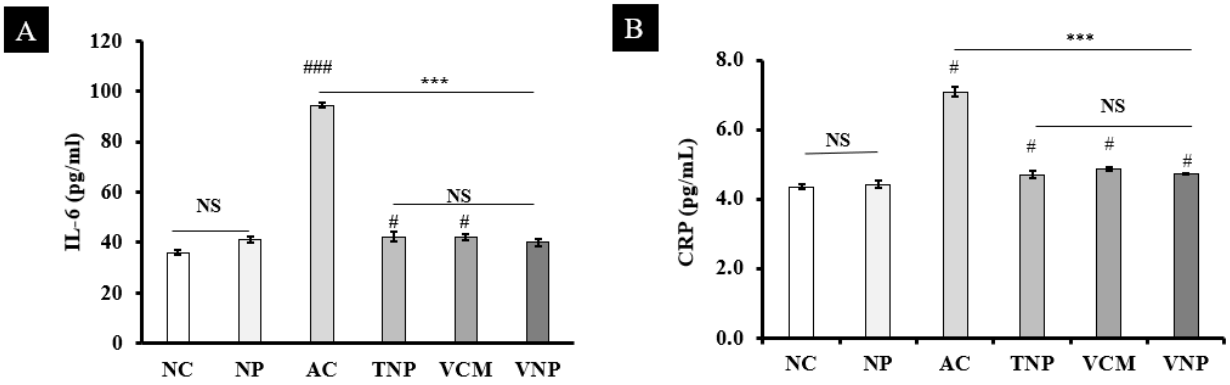

Figure 35 Impact of AgNPs and vancomycin on *S. aureus* infected male Wistar rat. **A.** IL-6, **B.** CRP. NC = Normal control, NP = Only nanoparticles, AC = Arthritis control, TNP = Treated with AgNPs, VCM = Treated with vancomycin, VNP = Treated with AgNPs and vancomycin. # p< 0.05, ## p<0.01, ### p<0.001 compared to the NC group; * p<0.05, ** p< 0.01, ***p< 0.001 compared to the AC group, NS= No significant difference.

5.29. Histological analysis

5.29.1. Knee joint

The histology of the knee joint of the NC group (**Figure 36A**) showed no inflammatory symptoms. The AC showed the classic signs of inflammation around the articular surface of the knee joints, lymphocyte infiltration, damaged articular cartilage and synovial membrane (**Figure 36B**). In comparison, rats in the treated group with NPs, VCM and VNP provide knee joint protection by reducing inflammation and necrosis. Minimal evidence of inflammation or joint destruction was found. In fact, the synovial membrane in the joints was almost like normal synovium, with few signs of synovial hyperplasia or other characteristics of inflammation (**Figure 36**).

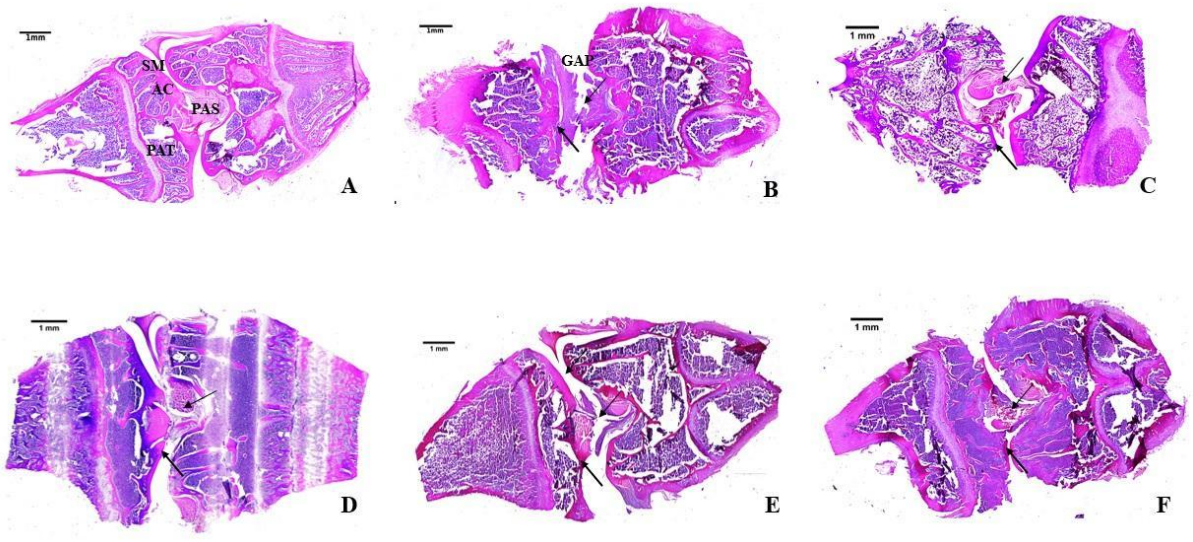

Figure 36 Whole slide histopathological examination of the knee joint (hematoxylin and eosin staining). **AC:** Articular cartilage; **SM:** Synovial membrane; **PAT:** Periarticular tissue; **PAS:** Periarticular cartilage. **A.** Normal control: lack of lymphocytes infiltration of synovium, intact periarticular tissue and articular bone. **B.** Arthritic control: prominent lymphocytic infiltration of the synovium (narrow arrow) with a clear gap (GAP) and damaged periarticular cartilage (broad arrow). **C.** Treated with AgNPs without bacteria: lack of lymphocytes infiltration of

synovium, intact periarticular tissue (narrow arrow) and slightly damaged periarticular cartilage (broad arrow). **D.** Treated with AgNPs: less gap, slightly damaged periarticular tissue (broad arrow) and articular cartilage (narrow arrow), **E.** Treated with VCM: less gap, mild lymphocyte infiltration of the synovium (broad arrow) and articular cartilage (narrow arrow). **F.** Treated with VNPs: mild infiltration of lymphocytes in the synovium, less gap and the damage in articular bone is quite negligible.

5.29.2. Liver

The NC group showed normal polyhedral hepatocyte cells. Each cell had a spherical, pale-stained nucleus and acidophilic cytoplasm. In contrast, the AC group showed varying degrees of degenerative changes in the hepatic lobules, characterized by granular degeneration, cell swelling, congestion in blood vessels, many dark nuclei of the irregular shape of hepatocytes, dark division nuclei of hepatocytes occurring around many manifold areas in the liver (**Figure 37**). However, In the treatment group, the degree of granular degeneration, cell swelling and congestion in blood vessels decreased. Moreover, when treatment was done in a combined form it was like the normal control group (**Figure 38**).

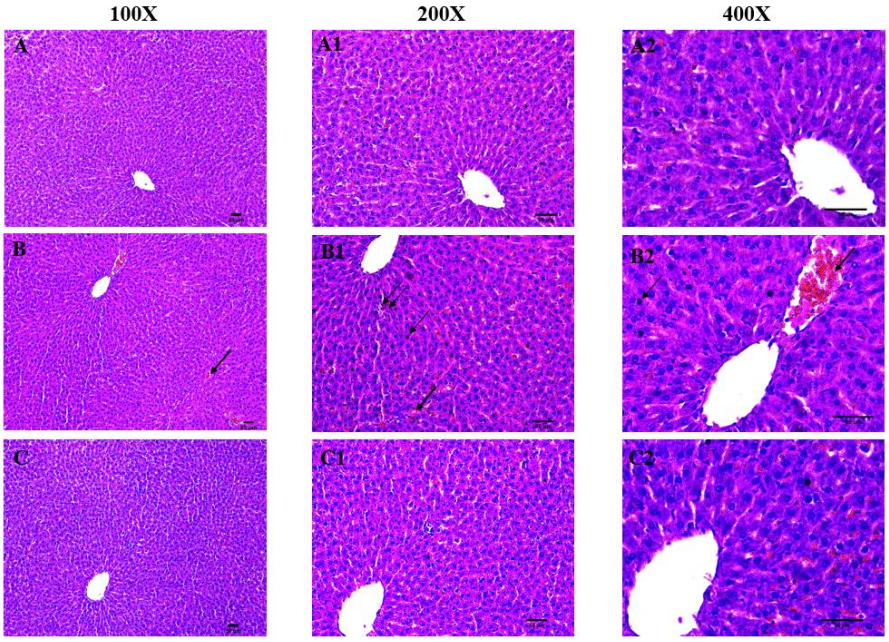

Figure 37 Histopathological examination of liver tissue under different magnifications (100X-400X). Normal control rat (**A-A2**); shows the normal hepatic architecture. Arthritis control rat (**B-B2**); **B:** congestion in blood vessels, **B1:** Double-headed arrow shows granular degeneration, narrow-headed arrow shows deeply stained nuclei, broad-headed arrow shows cell degeneration and some aggregation of inflammatory cells; **B2:** Narrow-headed arrow

shows deeply stained nucleus, broad-headed arrow shows vascular congestion. Only AgNPs treated rat without bacteria (**C-C2**); **C2:** normal hepatic structure was found.

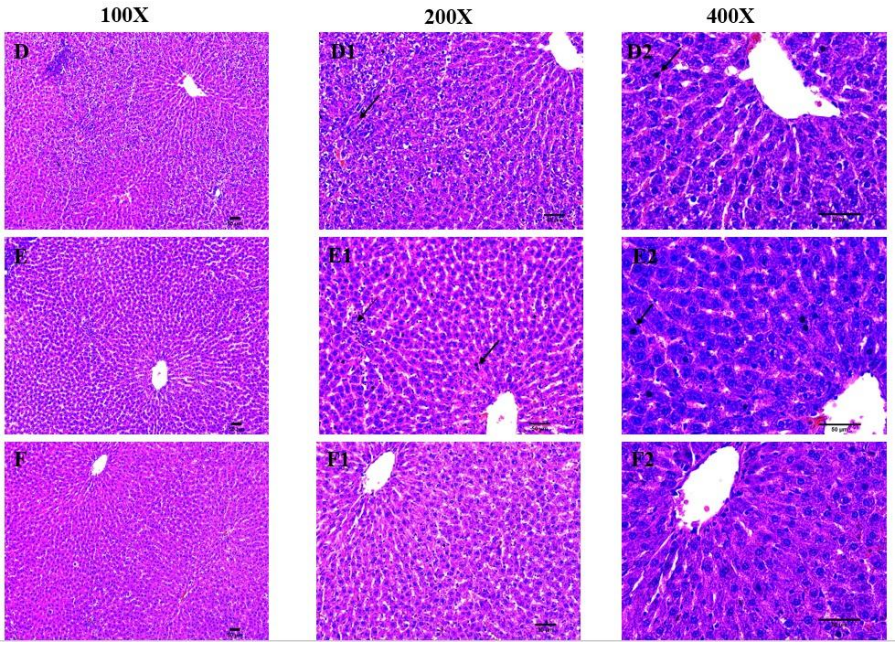

Figure 38 Histopathological examination of liver tissue under different magnifications (100X-400X). AgNPs treated rat (**D-D2**); **D1**: Broad-headed arrow shows moderate cell degeneration and some aggregation of inflammatory cells; **D2**: Deeply stained nuclei. VCN treated rat (**E-E2**); **E1**: Broad arrow shows dark division of nuclei of hepatocytes and narrow arrow shows moderate granular degeneration, **E2**: Deeply stained nuclei (broad arrow). VNPs treated rat (**F-F2**): Shows normal hepatic architecture.

5.28.3. Kidney

The NC group of rats has a normal architecture with normal glomeruli and tubules. Shrinkage of glomeruli, tubular lumen dilation and swollen tubular epithelial cells were found in the arthritis control group. Congested blood vessels were also found with aggregation of inflammatory cells due to bacterial infection (**Figure 38**). In the case of the treatment groups, it presents less inflammation and no observable histopathological changes are found. A relatively normal glomerular, renal tubule and interstitial tissue appearance were found in each case (**Figure 39**).

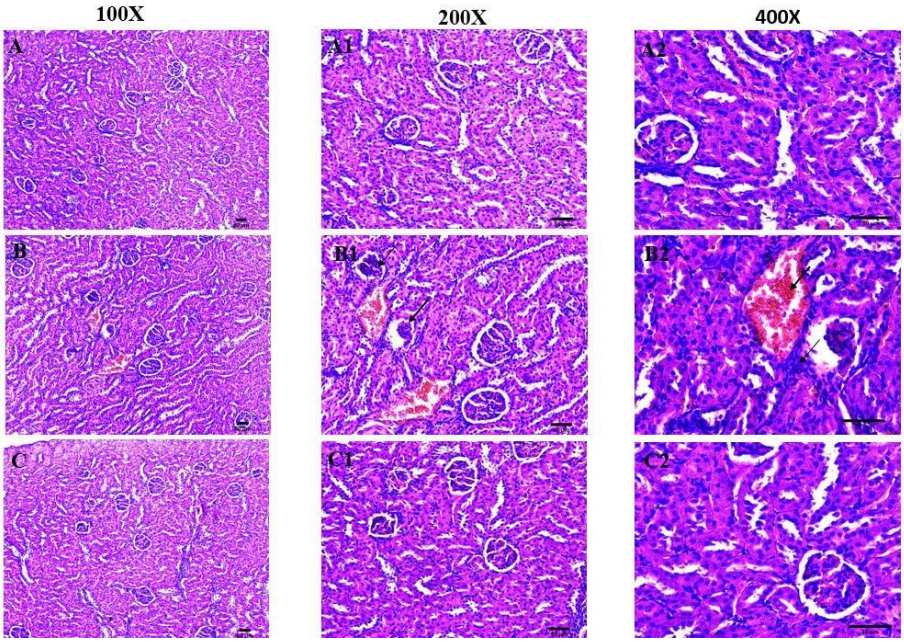

Figure 38 Histopathological examination of kidney tissue under different magnifications (100X-400X). Normal control rat (**A-A2**): Shows normal architecture of kidney tissue with normal glomeruli and tubules. Arthritis control rat (**B-B2**); **B1**: Narrow-headed arrow shows glomerular necrosis; broad-headed arrow shows shrinkage of glomeruli. Only AgNPs treated rat without bacteria (**C-C2**): No inflammatory sign was found. The normal architecture of the renal tissue was found.

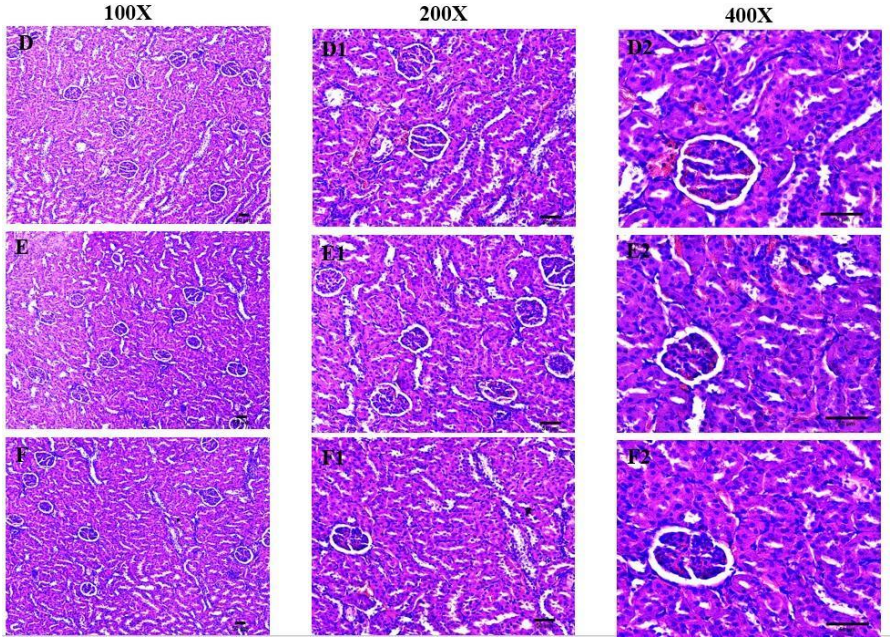

Figure 39 Histopathological examination of kidney tissue under different magnifications (100X-400X). AgNPs treated rat (**D-D2**): Demonstrating normal architecture of kidney tissue, less congestion with inflammatory cells was found. VCM treated rat (**E-E2**): Less inflammation was found with normal glomeruli and tubules. VNPs treated rat (**F-F2**): No

inflammatory symptoms was found and revealed almost complete prevention of histopathological alterations.

5.28.4. Spleen

The spleen tissue of the NC group has plenty of white pulp, red pulp, normal volume, moderate marginal layers and blood vessels. The AC group revealed significant red pulp congestion with inflammatory cells, thickened border areas and splenic hemorrhage with hemosiderin pigment deposition in the red pulp (**Figure 40**). However, treatment with AgNPs, VCM and VNPs can reduce these alterations of the white and red pulps and the associated pathological lesions (**Figure 41**).

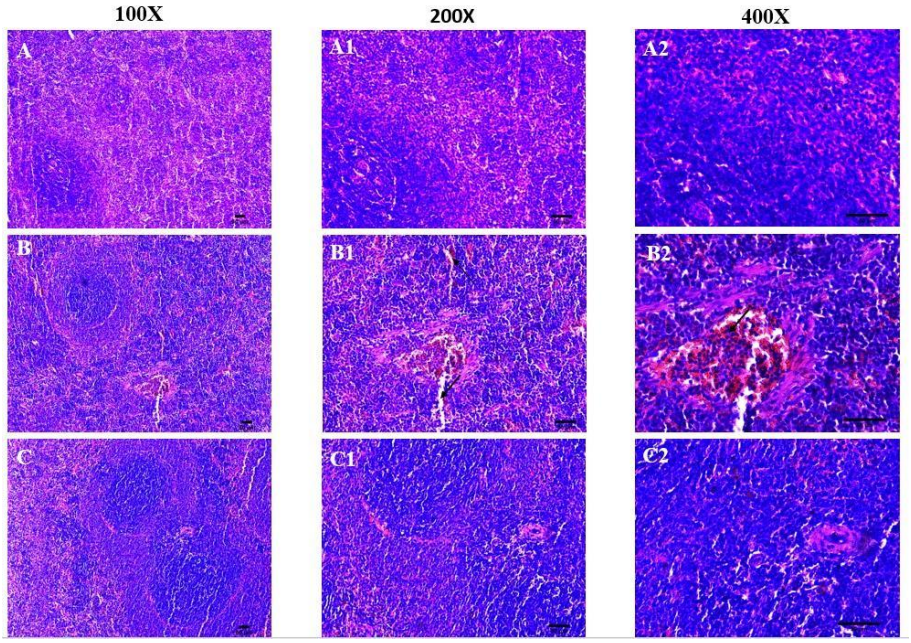

Figure 40 Histopathological examination of spleen tissue under different magnification (100X-400X). A. Normal control rat (**A-A2**): showing normal histology of both red and white pulp. Arthritis control rat (**B-B2**); **B1**: The narrow black arrow shows splenic hemorrhage with hemosiderin pigment deposition in the red pulp and the broad black arrow indicates deposition of hemosiderin pigment in the splenic parenchyma as well as inflammatory cells. Only AgNPs treated rat without bacteria (**C-C2**): No inflammatory sign is seen, it shows normal red pulp and white pulp.

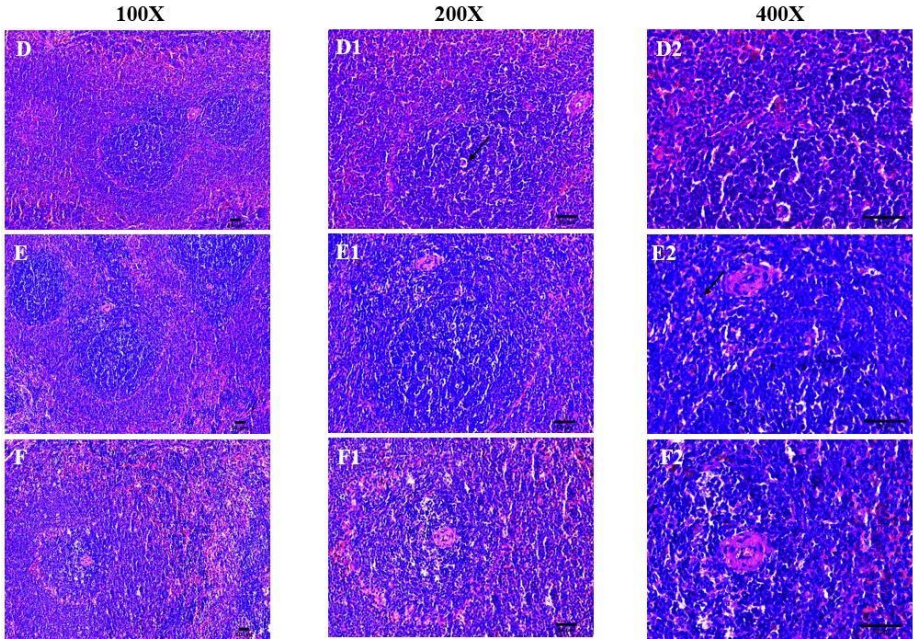

Figure 41 Histopathological examination of spleen tissue under different magnifications (100X-400X). AgNPs treated rat (**D-D1**): The black arrow denotes the loss of lymphoid cells and the presence of many tangible body macrophages within the periarteriolar lymphoid follicles of the spleen. VCM-treated rat (**E-E1**): The periarteriolar follicles were strongly stained and many tangible body macrophages were seen. VNPs treated rat (**F-F1**): No inflammatory sign was found in the red and white pulp.

5.30. Microscopic grading and scoring

The outcomes of lesion scoring were depicted in Figure **42**. In the liver tissue, there were notable findings of prominent hemorrhage, inflammation, abscesses and hepatic degeneration necrosis (HDN), all of which were significantly higher than those observed in both the normal control and treatment groups. Additionally, damage was observed in the kidney, spleen and knee joint within the arthritis control group. The kidney displayed significantly higher occurrences of renal tubular necrosis (RTN), inflammation, abscesses and hemorrhage. The spleen exhibited findings of hemorrhage, inflammation, abscesses and lymphoid depletion. Conversely, the knee joint showed periarticular tissue damage (PTD), articular cartilage damage (ACD), and lymphocyte infiltration. Microscopic scoring of the treatment group indicated a reduction in histopathological alterations in the tissues. Mild damage was noted in the groups treated with AgNPs, vancomycin and their combination.

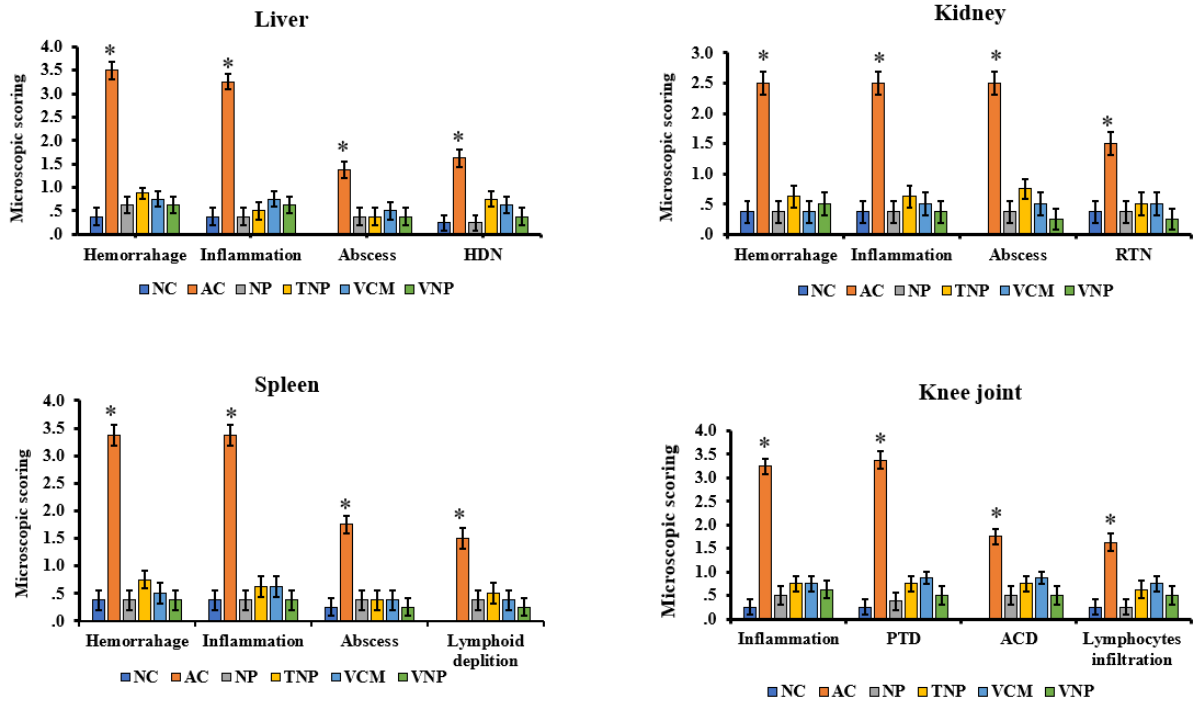

Figure 42 Qualitative analysis of liver, kidney, spleen and knee joint tissues. **HDN:** hepatic degeneration necrosis, **RTN:** renal tubular necrosis**, PTD:** periarticular tissue damage, **ACD:** articular cartilage damage, * p<0.05, ** p< 0.01, ***p< 0.001 compared to the NC group, NS= No significant difference.

6. Conclusion/Discussion

This work discusses the effective synthesis of AgNPs using a water-based extract from *S. aromaticum*, highlighting the simplicity and reliability of the method without the use of hazardous chemicals. The successful synthesis is confirmed by the noticeable colour change in the reaction mixture to brownish-yellow, indicative of the reduction of silver ions (Ag^{+}) to elemental silver (Ag^{0}). FTIR analysis reveals the presence of phytochemical components in the clove aqueous extract essential for NP formation. Similar observations in the change of the colour of the reaction mixture were reported when other plant extracts were used for the synthesis of AgNPs [44]. Parameters such as temperature, pH, incubation period, silver salt concentration and concentration of the plant extract have all been optimized in this study which act as critical factors that influence the successful synthesis of AgNPs in their optimal form. The blue shift indicated the formation of AgNPs of smaller size [13]. From the literature survey, it is found that the characteristic absorption peak of AgNPs occurs between 400-460 nm [45]. Studies have revealed that small-sized spherical AgNPs showed a peak at around 410 nm [46].

Hence, the NPs produced in this investigation exhibited a smaller size, which was additionally verified through TEM, XRD and AFM.

The study also shifts focus to the emergence and spread of pathogens, particularly *S. aureus*, highlighting the importance of characterizing the virulence and drug resistance profiles. A drastic increase in methicillin-resistant *S. aureus* (MRSA) is noted, associated with factors such as antibiotic use, socio-economic conditions and migration. The study employs various approaches to evaluate the genetic diversity of *S. aureus* strains, emphasizing the significance of the *mecA* gene in detecting MRSA. Increased bacterial resistance towards several antimicrobials makes vancomycin the drug of choice for the treatment of *S. aureus* MDR strains [47]. Several other *S. aureus* genes such as *nuc, pvl, SCC mec I* and *tsst-1* gene were also identified in this study to confirm their characteristics. *S. aureus* produces nuc gene which encodes the thermostable endonuclease of coagulase-positive *Staphylococcus* [48]. Additionally, they all tested positive for PVL, signifying the secretion of a potent cytotoxin that empowers them to eliminate host leukocytes [49].

The present study found that synthesized AgNPs has good antibacterial activity against *S. aureus*. Some researchers suggest that efficiency of the antibacterial activity of AgNPs is based on the size of AgNPs; smaller size of the particles leads to increased membrane permeability and cell destruction [50]. AgNPs release silver ions which damage bacterial membranes and lead to cell shrinkage and eventual death [51]. Then it interacts with sulphur present in the proteins as well as with the phosphorus containing compounds like DNA [52]. This study also investigated the mechanism of antibacterial activity of AgNPs where SEM and AFM results support bacterial membrane disruption, comet assay supports bacterial DNA damage and fluorescence studies indicate bacterial cell death.

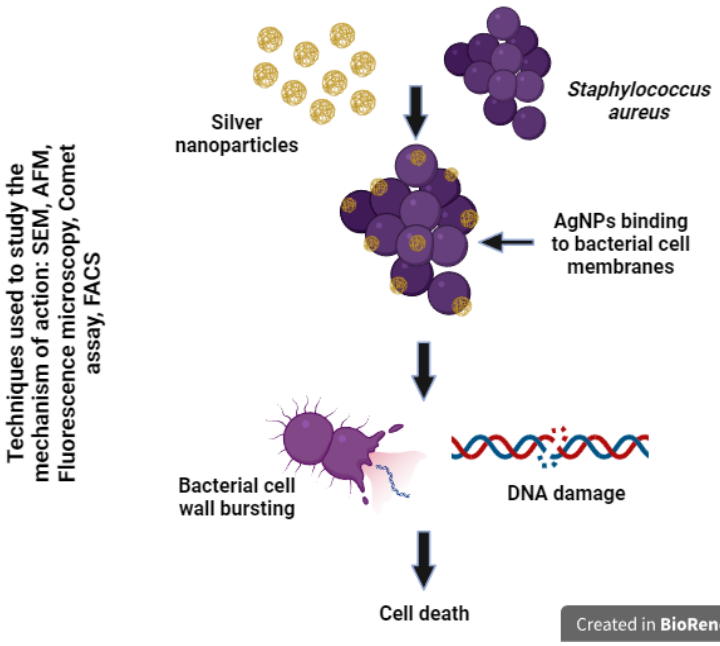
Techniques used to study the mechanism of action: SEM, AFM, Fluorescence microscopy, Comet assay, FACS
Silver nanoparticles
Staphylococcus aureus
AgNPs binding to bacterial cell membranes
Bacterial cell wall bursting
DNA damage
Cell death
Created in BioRender.com

Figure 43 Mechanism of action of the antibacterial activity of AgNPs.

The study also investigated that the AgNPs can degrade MG dye at a rate of 0.034±0.005 min^{-1} in the presence of sunlight. The removal efficiency of the AgNPs was compared with other NPs in former studies (**Table 9**). This photocatalytic degradation reaction mechanism is vital for the photocatalytic degradation process and developing more efficient and environmentally friendly methods for water treatment. The important possible reactions are summarized in the following equations (Xu et al., 2023) (**Figure 44**).

$$NPs + hv\ (photon) \rightarrow NPs\ (h^+ + e^-) \quad (1)$$

$$h^+ + MG\ Dye \rightarrow Oxidation\ of\ the\ MG\ dye\ molecules \quad (2)$$

$$h^+ + OH^-/H_2O \rightarrow \cdot OH \quad (3)$$

$$e^- + O_2 \rightarrow \cdot O_2^- \quad (4)$$

$$\cdot OH + \cdot O_2^- + dye \rightarrow degradable\ of\ MG \rightarrow production\ of\ less\text{-}toxic\ species \quad (5)$$

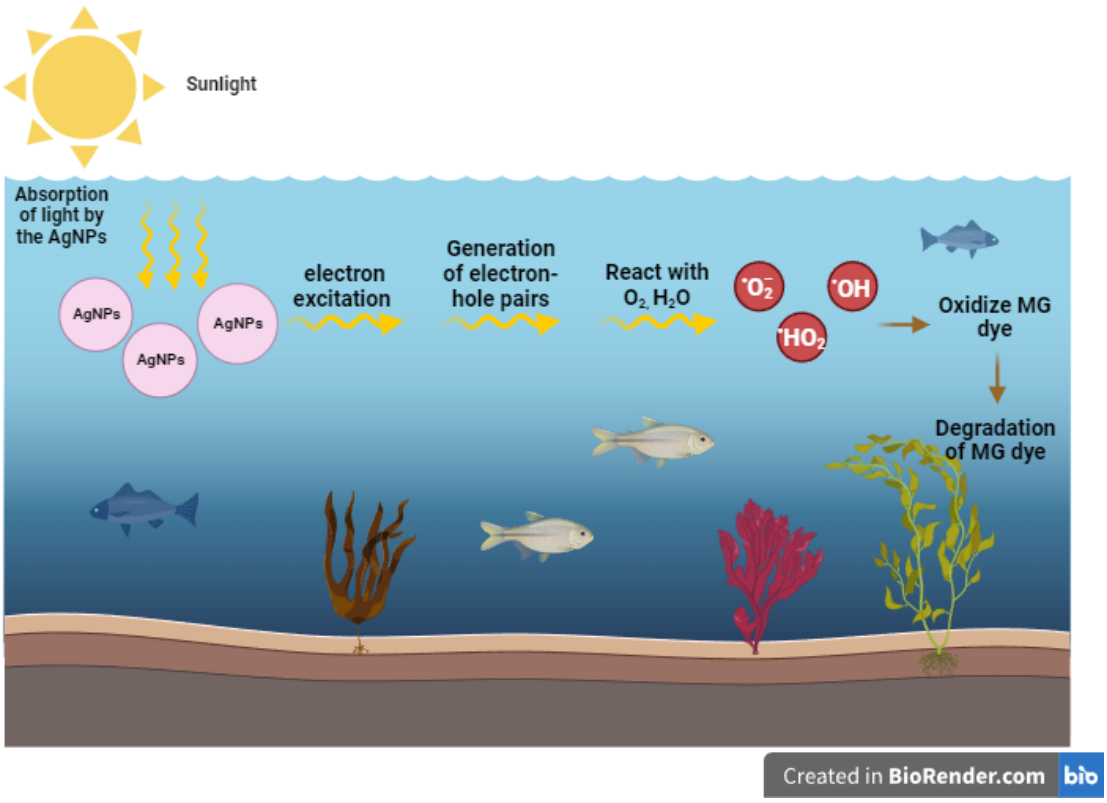

Figure 44 Proposed mechanism of photocatalytic degradation of MG dye

Table 9: Comparison of dye removal efficiency between green synthesized AgNPs and other NPs

Materials	**Method of preparation**	**Percentage of degradation**	**References**
Ag impregnated commercial titanium dioxide	liquid impregnation of $AgNO_3$ followed by heat treatment	84%	[53]
silver oxide nanoparticles	Biosynthesis method	94.7%	[54]
AgNPs	Green synthesis	91.66%	[21]
AgNPs	Green synthesis	69.23 %	[55]
AgNPs	**Green synthesis**	**97.21%**	**Present study**

In the context of septic arthritis induced in rats, this study explores the impact of AgNPs and vancomycin on tissue damage and organ-level infection, noting reduced damage when treated with AgNPs, vancomycin and their combination (**Figure 45**). Liver and kidney function markers, ALT, AST and creatinine, validate the protective effect of the treatments. Serum inflammatory factor IL-6 and CRP levels indicate reduced inflammation in the treatment group compared to the AC group. Overall, the study suggests the potential of AgNPs in combination with vancomycin as an antimicrobial agent and highlights their application in addressing antibiotic-resistant strains and inflammatory conditions.

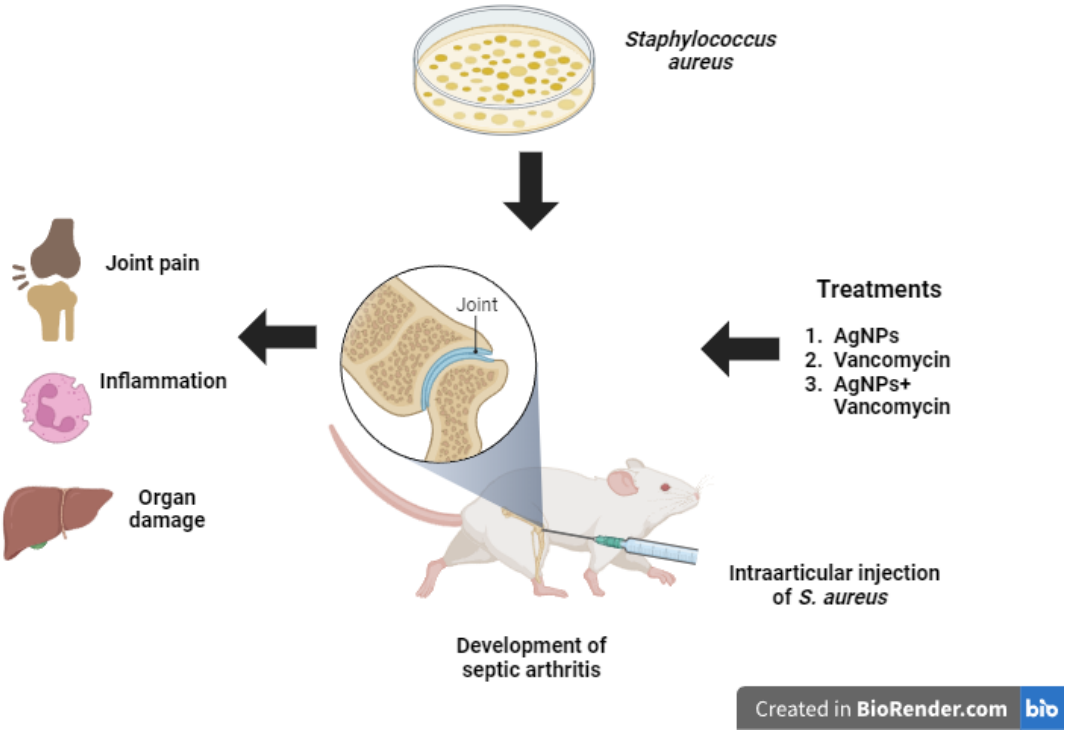

Figure 45 Study of the effect of AgNPs and vancomycin on septic arthritis

7. Significance of this study

The significance of this study lies in its revelation of the remarkable versatility of AgNPs across diverse applications. Firstly, the research showcases the effectiveness of AgNPs in combating bacterial infections, particularly in addressing *S. aureus*-mediated septic arthritis in a rat model. The demonstrated synergy of AgNPs with vancomycin emphasizes a potential therapeutic strategy for infectious diseases, contributing valuable insights to the field of medicine.

Moreover, the study extends the application spectrum of AgNPs to environmental concerns by highlighting their capability in organic dye elimination during wastewater treatment. This dual functionality of AgNPs in both antibacterial action and wastewater treatment underscores their potential as multifunctional agents with significant implications for public health and environmental sustainability.

In essence, the research not only broadens our understanding of AgNPs' versatility but also offers practical implications for addressing critical challenges in healthcare and environmental management. The findings open avenues for further exploration and application of AgNPs in diverse fields, potentially leading to the development of innovative and sustainable solutions.

8. Future directions

Based on these findings, the green-synthesized AgNPs demonstrate considerable potential in antimicrobial, anti-inflammatory and photocatalytic activities, suggesting their promising application across diverse fields such as biomedicine, wastewater treatment, biosensors and nanotechnology. A particularly encouraging avenue for exploration involves synergistically employing antibiotics and NPs to eradicate bacteria while concurrently mitigating the undesirable activation of the immune system. The robust degradation capabilities of AgNPs position them as potent agents in dye degradation approach. Consequently, a thorough exploration of these application possibilities warrants further investigation in the near future. This research may pave the way for innovative solutions addressing challenges in various domains, contributing to advancements in science and technology.

9. References

1. Hemlata; Meena, P.R.; Singh, A.P.; Tejavath, K.K. Biosynthesis of Silver Nanoparticles Using *Cucumis prophetarum* Aqueous Leaf Extract and Their Antibacterial and Antiproliferative Activity against Cancer Cell Lines. *ACS Omega* 2020, *5*, 5520–5528, doi:10.1021/acsomega.0c00155.

2. Muscia, G.C.; Carnevale, J.P.; Luczywo, A.; Victoria Peláez, M.; Rodríguez Ó Toole, A.; Buldain, G.Y.; Casal, J.J.; Asís, S.E. Synthesis, Anti-Tuberculosis Activity and QSAR Study of 2,4-Diarylquinolines and Analogous Polycyclic Derivatives. *Arab. J. Chem.* 2019, *12*, 932–945, doi:10.1016/j.arabjc.2018.10.003.

3. Tang, S.; Zheng, J. Antibacterial Activity of Silver Nanoparticles: Structural Effects. *Adv. Healthc. Mater.* 2018, *7*, 1–10, doi:10.1002/adhm.201701503.

4. Krithiga, N.; Rajalakshmi, A.; Jayachitra, A. Green Synthesis of Silver Nanoparticles Using Leaf Extracts of *Clitoria ternatea* and *Solanum nigrum* and Study of Its Antibacterial Effect against Common Nosocomial Pathogens . *J. Nanosci.* 2015, *2015*, 1–8, doi:10.1155/2015/928204.

5. Dobrucka, R.; Szymanski, M.; Przekop, R. The Study of Toxicity Effects of Biosynthesized Silver Nanoparticles Using *Veronica officinalis* Extract. *Int. J. Environ. Sci. Technol.* 2019, *16*, 8517–8526, doi:10.1007/s13762-019-02441-0.

6. Rautela, A.; Rani, J.; Debnath (Das), M. Green Synthesis of Silver Nanoparticles from Tectona Grandis Seeds Extract: Characterization and Mechanism of Antimicrobial Action on Different Microorganisms. *J. Anal. Sci. Technol.* 2019, *10*, doi:10.1186/s40543-018-0163-z.

7. El Faqer, O.; Bendiar, S.; Rais, S.; Elkoraichi, I.; Dakir, M.; Elouaddari, A.; Amrani, A. El; Oudghiri, M.; Mtairag, E.M. Phytochemical Characterization and Immunomodulatory Effects of Aqueous, Ethanolic Extracts and Essential Oil of

Syzygium Aromaticum L. on Human Neutrophils. *Sci. African* 2022, *18*, e01395, doi:10.1016/j.sciaf.2022.e01395.

8. Ferrand, J.; El Samad, Y.; Brunschweiler, B.; Grados, F.; Dehamchia-Rehailia, N.; Séjourne, A.; Schmit, J.L.; Gabrion, A.; Fardellone, P.; Paccou, J. Morbimortality in Adult Patients with Septic Arthritis: A Three-Year Hospital-Based Study. *BMC Infect. Dis.* 2016, *16*, 1–10, doi:10.1186/s12879-016-1540-0.

9. Jin, T.; Mohammad, M.; Pullerits, R.; Ali, A. Bacteria and Host Interplay in *Staphylococcus aureus* Septic Arthritis and Sepsis. *Pathogens* 2021, *10*, 1–25, doi:10.3390/pathogens10020158.

10. Aritonang, H.F.; Koleangan, H.; Wuntu, A.D. Synthesis of Silver Nanoparticles Using Aqueous Extract of Medicinal Plants' (*Impatiens balsamina* and *Lantana camara*) Fresh Leaves and Analysis of Antimicrobial Activity. *Int. J. Microbiol.* 2019, *2019*, doi:10.1155/2019/8642303.

11. Yasir, M.; Singh, J.; Manish Kumar Tripathi, P.S.; Shrivastava, R. Green Synthesis of Silver Nanoparticles Using Leaf Extract of Common Arrowhead Houseplant and Its Anticandidal Activity. *Pharmacogn. Mag.* 2017, *13*, 179–188, doi:10.4103/pm.pm_226_17.

12. Ndikau, M.; Noah, N.M.; Andala, D.M.; Masika, E. Green Synthesis and Characterization of Silver Nanoparticles Using *Citrullus lanatus* Fruit Rind Extract. *Int. J. Anal. Chem.* 2017, *2017*, doi:10.1155/2017/8108504.

13. Riaz, M.; Mutreja, V.; Sareen, S.; Ahmad, B.; Faheem, M.; Zahid, N.; Jabbour, G.; Park, J. Exceptional Antibacterial and Cytotoxic Potency of Monodisperse Greener AgNPs Prepared under Optimized PH and Temperature. *Sci. Rep.* 2021, *11*, 1–11, doi:10.1038/s41598-021-82555-z.

14. Loo, Y.Y.; Rukayadi, Y.; Nor-Khaizura, M.A.R.; Kuan, C.H.; Chieng, B.W.; Nishibuchi, M.; Radu, S. In Vitro Antimicrobial Activity of Green Synthesized Silver Nanoparticles against Selected Gram-Negative Foodborne Pathogens. *Front. Microbiol.* 2018, *9*, 1–7, doi:10.3389/fmicb.2018.01555.

15. Liou, J.W.; Hung, Y.J.; Yang, C.H.; Chen, Y.C. The Antimicrobial Activity of Gramicidin a Is Associated with Hydroxyl Radical Formation. *PLoS One* 2015, *10*, doi:10.1371/journal.pone.0117065.

16. Wu, Y.P.; Liu, X.Y.; Bai, J.R.; Xie, H.C.; Ye, S.L.; Zhong, K.; Huang, Y.N.; Gao, H. Inhibitory Effect of a Natural Phenolic Compound, 3-: P-Trans -Coumaroyl-2-Hydroxyquinic Acid against the Attachment Phase of Biofilm Formation of Staphylococcus Aureus through Targeting Sortase A. *RSC Adv.* 2019, *9*, 32453–32461, doi:10.1039/c9ra05883d.

17. Deng, S.P.; Zhang, J.Y.; Ma, Z.W.; Wen, S.; Tan, S.; Cai, J.Y. Facile Synthesis of Long-Term Stable Silver Nanoparticles by Kaempferol and Their Enhanced Antibacterial Activity Against *Escherichia coli* and *Staphylococcus aureus*. *J. Inorg. Organomet. Polym. Mater.* 2021, *31*, 2766–2778, doi:10.1007/s10904-020-01874-2.

18. Ananda, A.P.; Manukumar, H.M.; Krishnamurthy, N.B.; Nagendra, B.S.; Savitha, K.R. Assessment of Antibacterial Efficacy of a Biocompatible Nanoparticle PC@AgNPs against *Staphylococcus aureus*. *Microb. Pathog.* 2019, *126*, 27–39, doi:10.1016/j.micpath.2018.10.029.

19. Zhu Hui. Propidium Iodide Staining of Cells for FACS Analysis. 2012, *2*, 4–5.

20. Tan, P.; Tang, Q.; Xu, S.; Zhang, Y.; Fu, H.; Ma, X. Designing Self-Assembling Chimeric Peptide Nanoparticles with High Stability for Combating Piglet Bacterial Infections. *Adv. Sci.* 2022, *9*, 1–16, doi:10.1002/advs.202105955.

21. Chougule, S.S.; Gurme, S.T.; Jadhav, J.P.; Dongale, T.D.; Tiwari, A.P. Low Density Polyethylene Films Incorporated with Biosynthesised Silver Nanoparticles Using *Moringa oleifera* Plant Extract for Antimicrobial, Food Packaging, and Photocatalytic Degradation Applications. *J. Plant Biochem. Biotechnol.* 2021, *30*, 208–214, doi:10.1007/s13562-020-00584-7.

22. Batir-Marin, D.; Mircea, C.; Boev, M.; Burlec, A.F.; Corciova, A.; Fifere, A.; Iacobescu, A.; Cioanca, O.; Verestiuc, L.; Hancianu, M. In Vitro Antioxidant, Antitumor and Photocatalytic Activities of Silver Nanoparticles Synthesized Using *Equisetum species*: A Green Approach. *Molecules* 2021, *26*, 7325, doi:10.3390/molecules26237325.

23. Somasundaram, C.K.; Atchudan, R.; Edison, T.N.J.I.; Perumal, S.; Vinodh, R.; Sundramoorthy, A.K.; Babu, R.S.; Alagan, M.; Lee, Y.R. Sustainable Synthesis of Silver Nanoparticles Using *Marine algae* for Catalytic Degradation of Methylene Blue. *Catalysts* 2021, *11*, 1–13, doi:10.3390/catal11111377.

24. Moldovan, B.; David, L.; Vulcu, A.; Olenic, L.; Perde-Schrepler, M.; Fischer-Fodor, E.; Baldea, I.; Clichici, S.; Filip, G.A. In Vitro and in Vivo Anti-Inflammatory Properties of Green Synthesized Silver Nanoparticles Using *Viburnum opulus* L. Fruits Extract. *Mater. Sci. Eng. C* 2017, *79*, 720–727, doi:10.1016/j.msec.2017.05.122.

25. Shehensha, S.; Vijaya Jyothi, M. Anti-Inflammatory Activity of *Nigella sativa* Oil Mediated Silver Nanoparticles. *Pharmacogn. J.* 2020, *12*, 1086–1092, doi:10.5530/PJ.2020.12.153.

26. Sunanda Laxmi, P.; Vidyavathi, M.; Venkata, S.K.R. DoE Approach for Development of Localized Controlled Release Microspheres of Vancomycin for Treatment of Septic Arthritis. *Futur. J. Pharm. Sci.* 2021, *7*, doi:10.1186/s43094-021-00382-5.

27. Mal, P.; Dutta, S.; Bandyopadhyay, D.; Dutta, K.; Basu, A.; Bishayi, B. Gentamicin in Combination with Ascorbic Acid Regulates the Severity of *Staphylococcus aureus* Infection-Induced Septic Arthritis in Mice. *Scand. J. Immunol.* 2012, *76*, 528–540, doi:10.1111/j.1365-3083.2012.02766.x.

28. Mani, A.; Vasanthi, C.; Gopal, V.; Chellathai, D. Role of Phyto-Stabilised Silver Nanoparticles in Suppressing Adjuvant Induced Arthritis in Rats. *Int. Immunopharmacol.* 2016, *41*, 17–23, doi:10.1016/j.intimp.2016.10.013.

29. Ibrahim, K.E.; Al-Mutary, M.G.; Bakhiet, A.O.; Khan, H.A. Histopathology of the Liver, Kidney, and Spleen of Mice Exposed to Gold Nanoparticles. *Molecules* 2018, *23*, doi:10.3390/molecules23081848.

30. Hassanen, E.I.; Hussien, A.M.; Mehanna, S.; Ibrahim, M.A.; Hassan, N.H. Comparative Assessment on the Probable Mechanisms Underlying the Hepatorenal Toxicity of Commercial Imidacloprid and Hexaflumuron Formulations in Rats. *Environ. Sci. Pollut. Res.* 2022, *29*, 29091–29104, doi:10.1007/s11356-021-18486-z.

31. Jha, D.; Thiruveedula, P.K.; Pathak, R.; Kumar, B.; Gautam, H.K.; Agnihotri, S.; Sharma, A.K.; Kumar, P. Multifunctional Biosynthesized Silver Nanoparticles Exhibiting Excellent Antimicrobial Potential against Multi-Drug Resistant Microbes along with Remarkable Anticancerous Properties. *Mater. Sci. Eng. C* 2017, *80*, 659–669, doi:10.1016/j.msec.2017.07.011.

32. Tarmizi, Z.I.; Burhanuddin, M.F.B.; Shahrul, M.; Mokhtar, M.A.M.; Zhe, J.C.; Taib, S.H.M.; Sukri, S.N.A. Preparation and Characterization of Acetylated Starch Mediated Silver Nanoparticles: The Effect of Solution Ratio and Time-Varying Exposure. *J. Phys. Conf. Ser.* 2022, *2259*, doi:10.1088/1742-6596/2259/1/012005.

33. Mehta, B.K.; Chhajlani, M.; Shrivastava, B.D. Green Synthesis of Silver Nanoparticles and Their Characterization by XRD. *J. Phys. Conf. Ser.* 2017, *836*, doi:10.1088/1742-6596/836/1/012050.

34. Yu, C.; Tang, J.; Liu, X.; Ren, X.; Zhen, M.; Wang, L. Green Biosynthesis of Silver Nanoparticles Using *Eriobotrya japonica* (Thunb.) Leaf Extract for Reductive Catalysis. *Materials (Basel).* 2019, *12*, doi:10.3390/ma12010189.

35. Parlinska-Wojtan, M.; Kus-Liskiewicz, M.; Depciuch, J.; Sadik, O. Green Synthesis and Antibacterial Effects of Aqueous Colloidal Solutions of Silver Nanoparticles Using *Camomile terpenoids* as a Combined Reducing and Capping Agent. *Bioprocess Biosyst. Eng.* 2016, *39*, 1213–1223, doi:10.1007/s00449-016-1599-4.

36. Paulkumar, K.; Gnanajobitha, G.; Vanaja, M.; Pavunraj, M.; Annadurai, G. Green Synthesis of Silver Nanoparticle and Silver Based Chitosan Bionanocomposite Using Stem Extract of *Saccharum officinarum* and Assessment of Its Antibacterial Activity. *Adv. Nat. Sci. Nanosci. Nanotechnol.* 2017, *8*, doi:10.1088/2043-6254/aa7232.

37. Gaddam, S.A.; Kotakadi, V.S.; Sai Gopal, D.V.R.; Subba Rao, Y.; Varada Reddy, A. Efficient and Robust Biofabrication of Silver Nanoparticles by *Cassia alata* Leaf Extract and Their Antimicrobial Activity. *J. Nanostructure Chem.* 2014, *4*, doi:10.1007/s40097-014-0082-5.

38. Din, S.U.; Azeez, A.; Zain-ul-Abdin; Haq, S.; Hafeez, M.; Imran, M.; Hussain, S.; Alarfaji, S.S. Investigation on Cadmium Ions Removal from Water by a Nanomagnetite Based Biochar Derived from Eleocharis Dulcis. *J. Inorg. Organomet. Polym. Mater.* 2021, *31*, 415–425, doi:10.1007/s10904-020-01758-5.

39. Sharma, V.; Kaushik, S.; Pandit, P.; Dhull, D.; Yadav, J.P.; Kaushik, S. Green Synthesis of Silver Nanoparticles from Medicinal Plants and Evaluation of Their Antiviral Potential against Chikungunya Virus. *Appl. Microbiol. Biotechnol.* 2019, *103*, 881–891, doi:10.1007/s00253-018-9488-1.

40. Kamble, V.V.; Gaikwad, N.B. Fourier Transform Infrared Spectroscopy Spectroscopic Studies in *Embelia ribes* Burm. F.: A Vulnerable Medicinal Plant. *Asian J. Pharm. Clin. Res.* 2016, *9*, 41–47, doi:10.22159/ajpcr.2016.v9s3.13804.

41. Padalia, H.; Moteriya, P.; Chanda, S. Green Synthesis of Silver Nanoparticles from Marigold Flower and Its Synergistic Antimicrobial Potential. *Arab. J. Chem.* 2015, *8*, 732–741, doi:10.1016/j.arabjc.2014.11.015.

42. Guan, T.; Ding, L.G.; Lu, B.Y.; Guo, J.Y.; Wu, M.Y.; Tan, Z.Q.; Hou, S.Z. Combined Administration of Curcumin and Chondroitin Sulfate Alleviates Cartilage Injury and Inflammation via NF-KB Pathway in Knee Osteoarthritis Rats. *Front. Pharmacol.* 2022, *13*, 1–11, doi:10.3389/fphar.2022.882304.

43. Wang, J.; Gao, Y.; Hou, Y.; Zhao, F.; Pu, F.; Liu, X.; Wu, Z.; Fan, Y. Evaluation on Cartilage Morphology after Intra-Articular Injection of Titanium Dioxide Nanoparticles in Rats. *J. Nanomater.* 2012, *2012*, doi:10.1155/2012/452767.

44. Urnukhsaikhan, E.; Bold, B.E.; Gunbileg, A.; Sukhbaatar, N.; Mishig-Ochir, T. Antibacterial Activity and Characteristics of Silver Nanoparticles Biosynthesized from *Carduus crispus*. *Sci. Rep.* 2021, *11*, 1–12, doi:10.1038/s41598-021-00520-2.

45. Padalia, H.; Chanda, S. Synthesis of Silver Nanoparticles Using *Ziziphus nummularia* Leaf Extract and Evaluation of Their Antimicrobial, Antioxidant, Cytotoxic and Genotoxic Potential (4-in-1 System). *Artif. Cells, Nanomedicine Biotechnol.* 2021, *49*, 354–366, doi:10.1080/21691401.2021.1903478.

46. Ider, M.; Abderrafi, K.; Eddahbi, A.; Ouaskit, S.; Kassiba, A. Silver Metallic Nanoparticles with Surface Plasmon Resonance: Synthesis and Characterizations. *J. Clust. Sci.* 2017, *28*, 1051–1069, doi:10.1007/s10876-016-1080-1.

47. Monteiro, A. de S.; Pinto, B.L.S.; Monteiro, J. de M.; Ferreira, R.M.; Ribeiro, P.C.S.; Bando, S.Y.; Marques, S.G.; Silva, L.C.N.; Nunes Neto, W.R.; Ferreira, G.F.; et al. Phylogenetic and Molecular Profile of *Staphylococcus aureus* Isolated from Bloodstream Infections in Northeast Brazil. *Microorganisms* 2019, *7*, 1–14, doi:10.3390/microorganisms7070210.

48. Rosales-Villarreal, M.C.; Rocha-Guzmán, N.E.; Gallegos-Infante, J.A.; Moreno-Jiménez, M.R.; Reynoso-Camacho, R.; Pérez-Ramírez, I.F.; González-Laredo, R.F. Significance of Bioactive Compounds, Therapeutic and Agronomic Potential of Non-Commercial Parts of the Coffea Tree. *Biotecnia* 2019, *21*, 143–153, doi:10.18633/biotecnia.v21i3.1046.

49. Shil, A.; Bishayi, B.; Sikdar (ne'e Bhakta), M. Prevalence of Community-Associated *Staphylococcus aureus* Strains among University Students. *Prog. Heal. Sci.* 2021, *11*, 65–75, doi:10.5604/01.3001.0015.6400.

50. Krishnaraj, C.; Jagan, E.G.; Rajasekar, S.; Selvakumar, P.; Kalaichelvan, P.T.; Mohan, N. Synthesis of Silver Nanoparticles Using *Acalypha Indica* Leaf Extracts and Its Antibacterial Activity against Water Borne Pathogens. *Colloids Surfaces B Biointerfaces* 2010, *76*, 50–56, doi:10.1016/j.colsurfb.2009.10.008.

51. Naskar, A.; Lee, S.; Kim, K.S. Easy One-Pot Low-Temperature Synthesized Ag-ZnO Nanoparticles and Their Activity Against Clinical Isolates of Methicillin-Resistant *Staphylococcus aureus*. *Front. Bioeng. Biotechnol.* 2020, *8*, 1–8, doi:10.3389/fbioe.2020.00216.

52. Singh, D.; Rawat, D.; Isha Microwave-Assisted Synthesis of Silver Nanoparticles from *Origanum majorana* and *Citrus sinensis* Leaf and Their Antibacterial Activity: A Green Chemistry Approach. *Bioresour. Bioprocess.* 2016, *3*, doi:10.1186/s40643-016-0090-z.

53. Saha, S.; Wang, J.M.; Pal, A. Nano Silver Impregnation on Commercial TiO 2 and a Comparative Photocatalytic Account to Degrade Malachite Green. *Sep. Purif. Technol.* 2012, *89*, 147–159, doi:10.1016/j.seppur.2012.01.012.

54. Aiswariya, K.S.; Jose, V. Bioactive Molecules Coated Silver Oxide Nanoparticle Synthesis from *Curcuma zanthorrhiza* and HR-LCMS Monitored Validation of Its Photocatalytic Potency Towards Malachite Green Degradation. *J. Clust. Sci.* 2022, *33*, 1685–1696, doi:10.1007/s10876-021-02099-0.

55. Lakshmi, S.P.; Dhanya, S.; Sheeba, D. Photocatalytic Degradation of Malachite Green Using Silver Nanoparticles Synthesised from Gooseberry Extract. *J. Chem. Mater. Res.* 2016, *5*, 68–73.